Lisa Dreier, BSc

$CuInS_2$ Nanoparticle Preparation with Colloidal Methods, Characterization Ligand Exchange and Possible Applications in Hybrid Solar Cells

Masterarbeit

zur Erlangung des akademischen Grades

Diplom-Ingenieurin

Masterstudium Technische Chemie

eingereicht an der

Technischen Universität Graz

Betreuer

Assoc. Prof. Dipl.-Ing. Dr. techn. Gregor Trimmel

Institut für Chemische Technologie von Materialien

Graz, November, 2014

EIDESSTATTLICHE ERKLÄRUNG

Ich erkläre an Eides statt, dass ich die vorliegende Arbeit selbstständig verfasst, andere als die angegebenen Quellen/Hilfsmittel nicht benutzt, und die den benutzten Quellen wörtlich und inhaltlich entnommenen Stellen als solche kenntlich gemacht habe. Das in TUGRAZonline hochgeladene Textdokument ist mit der vorliegenden Masterarbeit identisch.

AFFIDAVIT

I declare that I have authored this thesis independently, that I have not used other than the declared sources/resources, and that I have explicitly indicated all material which has been quoted either literally or by content from the sources used. The text document uploaded to TUGRAZonline is identical to the present master‘s thesis.

Datum / Date Unterschrift / Signature

Abstract

Organic inorganic hybrid solar cells are an interesting alternative to silicon solar cells. They combine the advantages of the organic and inorganic materials, respectively. A very important benefit of nanoparticles is the possibility to change their properties by tuning their size and shape. $CuInS_2$ nanoparticles have good optical properties, while being non-toxic. Thus, the use of $CuInS_2$ nanocrystals in solar cells has a good future prospective. Therefore, their application is investigated.

In this work $CuInS_2$ nanoparticles were synthesized via colloidal methods using different copper and indium precursors as well as different cappers and sulfur sources. The influence of the used amount of 1-dodecanethiol on side products and gel formation was examined. The prepared nanoparticles were characterized using x-ray diffraction analysis and transmission electron microscopy.

The oleic acid and 1-dodecanethiol ligand shell was subjected to a ligand exchange step. Ligand exchange with pyridine, butylamine and 1,2-ethanedithiol was performed and the ligand shell was investigated with simultaneous thermal analysis and infrared spectroscopy.

For the preparation of hybrid solar cells, the previously synthesized $CuInS_2$ nanoparticles were used as acceptor phase. The conductive polymer PSiF-DBT was used as donor phase. The influence of the ligand exchange, as well as the stoichiometry (copper to indium molar ratio) on the performance of hybrid solar cells was investigated. Solar cells were prepared in a bulk heterojunction assembly and in an inverse bulk heterojunction assembly.

Characteristic parameters of the solar cells were determined by recording current voltage curves. The active layer was analyzed with UV/VIS spectroscopy and photoluminescence quenching experiments. Furthermore, film thickness and roughness measurements were conducted.

Kurzfassung

Organisch-anorganische Hybridsolarzellen stellen eine interessante Alternative zu Siliziumsolarzellen dar. Sie vereinbaren die Vorteile der organischen und anorganischen Materialien. Einer der großen Vorzüge von Nanopartikel ist die Möglichkeit ihre Eigenschaften durch die Größe und Form einzustellen. $CuInS_2$ Nanopartikel, haben gute optische Eigenschaften und sind nicht giftig, weshalb ihre Anwendung in Solarzellen untersucht wird.

In dieser Arbeit wurden $CuInS_2$ Nanopartikel über kolloidale Methoden hergestellt. Hierfür wurden unterschiedliche Kupfer- und Indium-Präkursoren sowie unterschiedliche Liganden und Schwefelquellen verwendet. Der Einfluss der für die Synthese verwendeten 1-Dodecanthiol Menge auf Nebenprodukte und Gelbildung wurde eingehend erforscht. Die synthetisierten Nanopartikel wurden mittels Röntgendiffraktometrie und Transmissionselektronenmikroskopie untersucht.

An den zuvor synthetisierten Nanopartikeln, deren ursprüngliche Ligandenhülle aus Ölsäure und 1-Dodecanthiol bestand, wurde ein Ligandenaustausch mit Pyridin, Butylamin und 1,2-Ethandithiol durchgeführt. Die Ligandenhülle wurde mittels Infrarotspektroskopie und simultaner Thermoanalyse charakterisiert.

Für die Herstellung von Hybridsolarzellen wurden die präparierten $CuInS_2$ Nanopartikel als Akzeptormaterial verwendet. Als Donormaterial diente das leitende Polymer PSiF-DBT. Es wurden sowohl der Einfluss der unterschiedlichen Ligandenhüllen als auch der Einfluss der Stöchiometrie (Kupfer zu Indium Verhältnis) auf die Leistung der Solarzellen untersucht.

Die Solarzellen wurden mit Hilfe von Strom-Spannungskurven charakterisiert. Schichtdicke und Rauigkeit der Aktivschichten wurden mit einem Profilometer bestimmt. Weiters wurden die Aktivschichten mittels UV/VIS Spektroskopie und Fluoreszenzspektroskopie analysiert.

Acknowledgements

I would like to thank Assoc. Prof. Dipl.-Ing. Dr. techn. Gregor Trimmel for providing me with the possibility of writing my master thesis in his working group as well as for supervising me during my research. Furthermore, I would like to thank Univ.-Prof. Dipl.-Ing. Dr. techn. Stelzer, the head of the Institute for Chemistry and Technology of Materials.

A special thanks goes to Dr. Verena Harum and Dr. Thomas Rath for the helpful discussions and idea input. Thank you for all your support during my work.

I would like to thank all the members of the Institute for Chemistry and Technology of Materials for the friendly atmosphere and help. Especially I want to thank the people in the photovoltaic group and those in my office. It was a pleasure to work with all of you.

Moreover, I would like to thank Birgit Kunert and Ao. Univ.-Prof. Dipl.-Ing. Dr. techn. Franz Mautner for the XRD measurements, Amtsrätin Ing. Josefine Hobisch for the STA analysis and DI Dr. Karin Wewerka for the TEM images.

Thank you to my family, especially my parents, who supported me during the whole course of my studies. This would not have been possible without you.

Contents

1 Introduction

1.1 Energy Consumption and CO_2 Emissions

During the last century the CO_2 concentration in the air has increased drastically. The high CO_2 concentrations in the atmosphere will lead to higher average temperatures. In order to minimize this effect on the climate, the anthropogenic CO_2 emissions in the future have to be reduced.[1]

A huge amount of the anthropogenic CO_2 emissions is due to fossil fuels. In addition to that, fossil resources are diminishing, while the energy demand is increasing (see figure 1). Therefore, the research on alternative materials and technologies for the production of clean energy is of uttermost importance.[2]

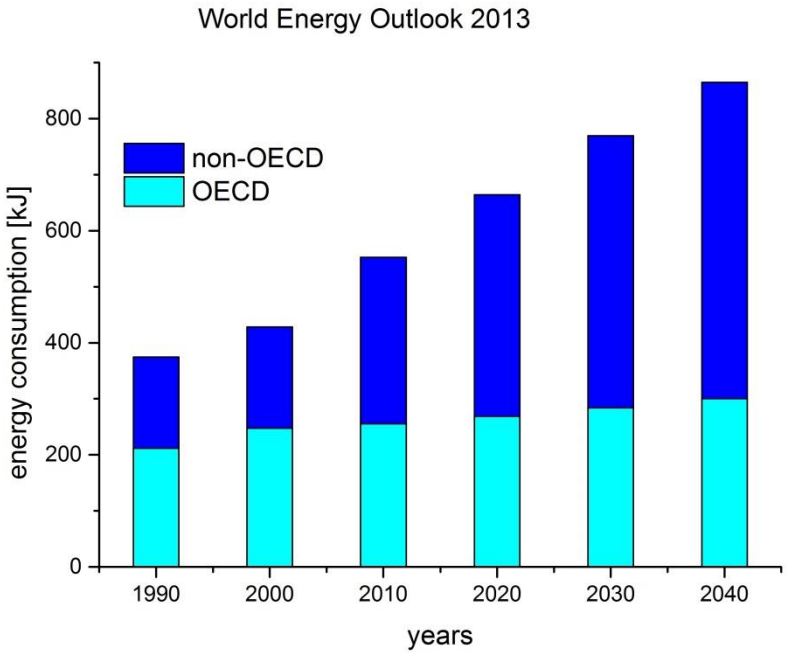

Figure 1: world energy consumption outlook 2013[3]

In 2012 the production of energy from renewable resources within the EU-28 only accounted for around 22% of the total primary energy production. Even though there was a fast increase in solar energy production in the last years, the share of solar energy of total renewable energy production in the EU-28 in 2012 was only around 5%.[4]

1.2 History of Solar Energy

The energy of the sun is the earliest used energy source. Many ancient cultures worshipped the sun as a powerful God.[5] The first use of solar energy dates back to the 7th century B.C., when the rays of the sunlight were concentrated by magnifying glasses in order to make fire and burn ants.[6]

It is said that in 212 B.C the Greek scientist and philosopher Archimedes used concave metallic mirrors to concentrate the sunlight on the attacking Roman ships in order to set them on fire. The Romans, who could not see what they were fighting against, believed to be combating with Gods. However, the technology to manufacture mirrors had not been invented at that time. Therefore, many scientists criticized the story as a myth. On the other hand, many historians believe that Archimedes used the shields from soldiers instead of mirrors for focusing the sun.[5]

It is documented that in the 2nd century A.D. the Chinese used burning mirrors in order to light torches for religious purposes. Between the 1st and the 4th century the Romans built their famous bathhouses with large south facing windows to let in the warmth of the sun. The first solar collectors were built in the late 18th century.[6]

In 1839 Henri Becquerel discovered, that materials can be influenced by light. He found out, that the conductivity of certain metals, such as selenium, changes upon illumination.[7]

In 1954, the first silicon photovoltaic cell was developed at Bell laboratories. It had a conversion efficiency of 6%. This type of solar cell was used for power supply of a space satellite in 1958. It was also detected in Bell laboratories, that the light sensitivity of silicon can be enhanced through the addition of impurities.[8]

The first solar cells consisted of crystalline silicon. Nowadays single-crystalline, polycrystalline and amorphous silicon is used in solar cells.[8]

However, there are also many other semiconducting materials such as Gallium arsenide, Cadmium telluride and Copper indium diselenide being applied in solar cells.[8]

1.3 Aim of This Thesis

Organic inorganic hybrid solar cells are an alternative to silicon solar cells. In this concept, organic conducting polymers are used as electron donors that absorb the sun light. While inorganic nanoparticles act as electron acceptors. However, the inorganic nanoparticles can also absorb light.

The aim of this thesis is the synthesis of copper indium disulfide nanoparticles via colloidal method and the characterization of the particles. Various preparation methods using different metal salts, sulfur sources and capping agents are compared. The synthesized CIS nanocrystals are investigated using x-ray diffraction analysis, UV/VIS spectroscopy and thermo-gravimetric analysis.

The prepared nanocrystals are introduced into organic inorganic hybrid solar cells. The influence of ligand exchange as well as the influence of the polymer to nanoparticle weight ratio and the copper to indium molar ratio on the device performance is investigated. The performance of the prepared solar cells is determined through I/V characteristics.

Furthermore, the layers are characterized by determining their thickness and roughness. Fluorescence experiments are carried out, in order to determine the photoluminescence quenching of the polymer by the nanoparticles.

The following chapters deal with the basics of solar cell materials and the physical principles of solar cells. The electrical properties and characteristic parameters of a solar cell are discussed as well. Additionally, the chapter contains an introduction into hybrid solar cells and a discussion on the fundamentals of material preparation for this type of devices.

In chapter 2, the experimental work that has been conducted is described. Thus, the different nanoparticle preparation methods, as well as the solar cell preparation and the ligand exchange processes are covered in that chapter.

The results and a discussion thereof can be found in chapter 3.

1.4 Basics of Solar Cells

Solids can be classified into different groups depending on their electrical conductivity.[9]

If a valence band is completely filled with electrons the electrons cannot move. Therefore, there is no electrical conductivity. In order for materials to be conducting, they have to contain bands that are only partially filled with electrons.[9]

Materials where the valence band and the conduction band overlap or the band gap is smaller than 0.1 eV are called electrical conductors (see Figure 2). Due to the overlapping of the bands or the very small band gap, a part of the valence electrons moves into the conduction band. Therefore, both bands are only partially filled with electrons and are thus able to conduct electrons. Examples for electrical conducting materials are metals such as lithium and beryllium.[9]

Insulators contain a fully filled valence band. Furthermore, the valence band is separated from the conduction band by a band gap of more than 4 eV. This energy barrier is too high for the electrons to be able to overcome it. Therefore, the electrons in this type of material cannot move freely. Thus, no electrical conduction takes place. Diamond, with a band gap of 5.2 eV, is an example for insulating materials.[9]

In semiconductors the band gap is lower than 4 eV. Therefore, the electrons can be transferred into the conduction band via the input of a relatively small amount of energy, such as for example heat. Thus, the valence band and the conduction band are both partially filled with electrons and the material turns into a conducting material.[9]

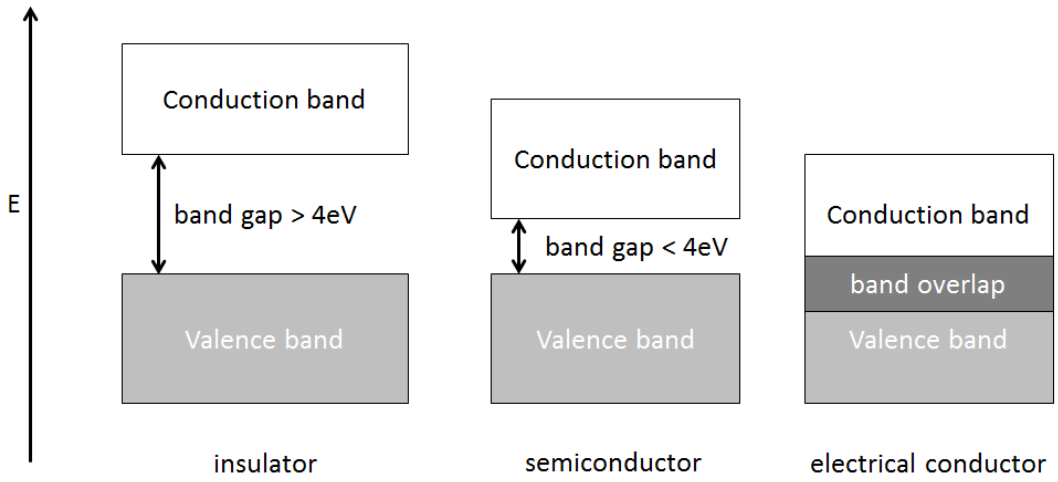

Figure 2: Energy diagram of different types of materials

Some examples for semiconductor materials are silicon and germanium as well as combined materials like GaAs, InAs, GaP and InP.

For silicon the band gap is 1.1 eV at room temperature. However, if a silicon atom is replaced by a pentavalent like phosphorous, the fifth electron is not covalently bound in the crystal. Thus, it can move freely. This electron then requires only 0.05 eV in order to be detached. This type of doping is named n-type doping. On the other hand, a silicon atom can also be replaced by a trivalent atom like boron. This atom can gather a fourth electron, creating a hole that allows electrons to move more freely. This type of doping is called p-type doping. Doping considerably increases the amount of free electrons and hence the conductivity of the semiconducting material.[8,10]

The interface between an n-doped and a p-doped region in a silicon crystal is called p/n junction. In the n-doped region there is an excess of electrons. Due to the concentration gradient the electrons start to diffuse into the p-doped region. Each electron leaves a positively charged atom behind that acts as a stationary positive charge. As soon as an electron encounters a hole in the p-doped region it occupies the empty space and thus can be considered a stationary charge as well. An electric field evolves due to the increasing amount of stationary charges, which leads to a field current in the opposite direction. An equilibrium develops, yielding a so called space-charge region.[11]

If light with energy higher than the band gap energy is absorbed by a semiconductor, each photon lifts an electron from the valence band into the conduction band. Thus, an electron and a hole are generated. The lower the band gap energy of a semiconductor is, the more electric current can be achieved. The developed electron/hole pairs are held together by Coulomb forces. However, they are separated by the electric field in the space charge region. The electrons are brought to the n-region while the holes are brought to the p-region. The thereby generated photocurrent can be gathered by the respective electrodes. The created current is influenced by the intensity of the incident light as well as the nature of the semiconductors in the cell.[8,11]

1.5 Hybrid Solar Cells

The majority of solar cells on the market are silicon based solar cells.[12] Crystalline silicon solar cells reach efficiencies up to 25%.[13] However, they consist of very expensive materials that require high temperatures and energy intensive techniques for their production. Therefore, a lot of research on other types of solar cells is being performed. There are dye sensitized solar cells, small molecule thin film solar cells, polymer/fullerene bulk heterojunction solar cells, and organic/inorganic hybrid solar cells, just to name a few.[12]

Organic inorganic hybrid solar cells combine the properties of organic and inorganic materials. The advantages that arise from the organic conducting polymer are that the materials are cheap, easy to prepare and have a high absorption coefficient. As a result of the high absorption coefficients, very thin films still absorb a high enough portion of the solar spectrum. Thus, a smaller amount of material is necessary for solar cell production. The chemical and physical stability, good electron mobility and tunable light absorption properties as a result of the quantum confinement effect, are due to the inorganic nanoparticles. Amongst others, CdSe, TiO_2, PbS, ZnO, PbSe, $CuInS_2$ and spherical Si nanocrystals are being investigated as inorganic materials for hybrid solar cells. Examples for organic materials are polymers such as polythiophenes, poly-para-phenylenevinylenes and a wide range of other conjugated polymers.[14,15,16] The first polymer nanocrystal hybrid solar cell consisted of CdSe nanoparticles and the polymer poly(2-methoxy-5-(2'-ethyl)-hexyloxy-p-

phenylenevinylene (MEH-PPV). It was reported in 1996.[17] The best power conversion efficiency reached with hybrid solar cells so far is 5.5% reported by Z. Liu, Y. Sun et al. using the low band gap polymer PDTPBT together with PbS_xSe_{1-x} nanocrystals.[18] The efficiencies achieved for example with organic photovoltaic cells consisting of a polymer/fullerene heterojunction are still considerably higher than those of hybrid solar cells. This discrepancy is mostly due to problems with surface chemistry and nanomorphology of the active layer in hybrid solar cells.[16]

1.6 Principle of Hybrid Solar Cells

When a solar cell is exposed to light, photons are absorbed by the polymer and an electron is excited from the highest occupied molecular orbital (HOMO) to the lowest unoccupied molecular orbital (LUMO). Thus, an electron/hole pair (exciton) is generated. The exciton then diffuses to the polymer/nanoparticle interface where the charges are separated. Since the electron and the hole are bound together by Coulomb forces, energy is needed in order to separate the charges. This force is supplied by the difference of energy levels of the LUMO of the polymer and the conduction band of the inorganic nanoparticles. The electron is transferred from the polymer to the nanoparticle. Hence, they are referred to as donor and acceptor, respectively. The hole stays with the polymer. The charge is then transported to the corresponding electrode where it is collected. For a demonstration of the electron pathways in a hybrid solar cell see figure 3. In hybrid solar cells the inorganic nanoparticles can also absorb light. The holes that are generated through the excitation of the electrons in the nanoparticles are transferred to the polymer. Thus, a hole transfer occurs in the opposite direction than the electron transfer.[19,20,16]

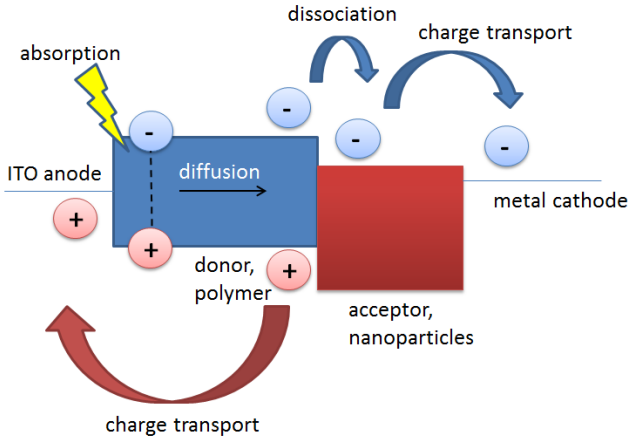

Figure 3: principle of a hybrid solar cell[16]

The properties of the materials that are used for hybrid solar cells are very essential for the cell efficiency. The electronic composition and the hole mobility of the donor material are of great importance. Especially the band gap and the HOMO and LUMO levels with regard to those of the acceptor material are of particular interest.[16] Figure 4 shows the chemical structures of some examples for polymers used in hybrid solar cells.

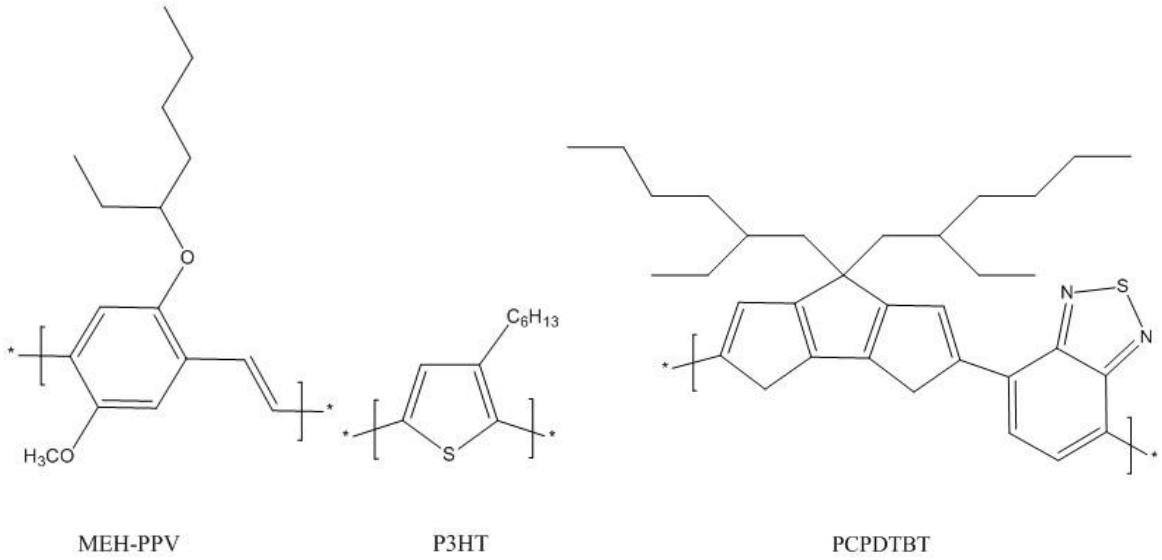

Figure 4: structures of some examples for polymers used in hybrid solar cells

One of the most important advantages of the use of inorganic semiconducting nanoparticles as acceptors in hybrid solar cells is the possibility to tune their band gap by modifying the size of the nanocrystals. In order to achieve good photon

absorption, the band gap of the material has to be as low as possible, permitting the utilization of a larger part of the solar spectrum. On the other hand, the open circuit voltage (V_{oc}) of a cell may be influenced by the difference in the HOMO of the polymer and the conduction band of the nanoparticles. V_{oc} has a greater value if the conduction band of the acceptor phase lies higher.

Another factor that needs to be considered is the difference in energy levels between the HOMO of the polymer and the valence band of the nanoparticles. Since the inorganic material also functions as an absorber, the dissociation of the excitons generated in the nanoparticle is easier if there is a difference in those energy levels. Figure 5 shows the calculated ideal energy level values for the materials in a hybrid solar cell.[16]

However, there are still some other factors that have to be considered for the selection of an acceptor material, such as the abundance and cost of the nanocrystals. Additionally, there has to be a balance between the electron and hole mobility as well as a successful nanomorphology between the phases of the two materials.[16]

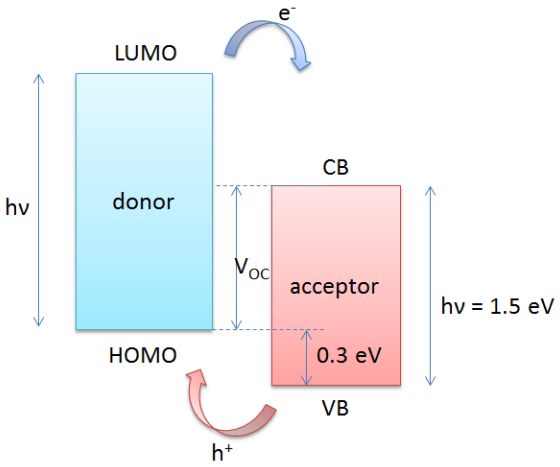

Figure 5: schematics of the energy levels of an ideal material system for a hybrid photovoltaic cell[16]

1.7 Device Architecture of a Hybrid Solar Cell

Most hybrid solar cells are fabricated on a transparent substrate like glass or Polyethylene terephthalate (PET). Usually the anode consists of indium tin oxide (ITO), an oxide that is transparent in the visible range and conducting.[16]

Generally Poly(3,4-ethylenedioxythiophene)-poly(styrenesulfonate) (PEDOT:PSS), a conductive polymer, is spin coated on top of the anode for surface smoothening of the anode. Additionally, it functions as a hole transporting layer and blocks the excitons.[16] Figure 6 shows the structure of the polymer.

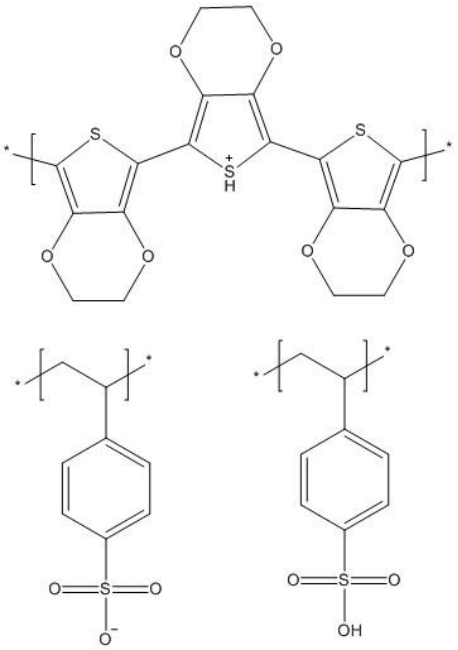

Figure 6: structure of the conductive polymer PEDOT:PSS

The active layer consisting of a polymer and the nanoparticles is applied on top of the PEDOT:PSS coating. This may be achieved via spin coating or doctor blading.[16] Formerly the active layer of heterojunction solar cells was constructed as a bilayer. Thus, there was a polymer layer and a nanoparticle layer on top of each other. However, the generated excitons only diffuse for a certain length (about 10 nm) until recombination occurs. Therefore, in a bilayer construction most of the excitons are generated too far away from the donor acceptor interface to still be able to reach it. The problem was solved by the development of one layer containing the donor as well as the acceptor. Here the nanoparticles are dispersed in the polymer phase, forming an interpenetrating layer. As a result, the distance between the place where

the excitons are formed and the nearest donor acceptor interface is much shorter. This construction type is called bulk heterojunction solar cell.[21] Figure 7 shows the schematics of the two described active layer systems.

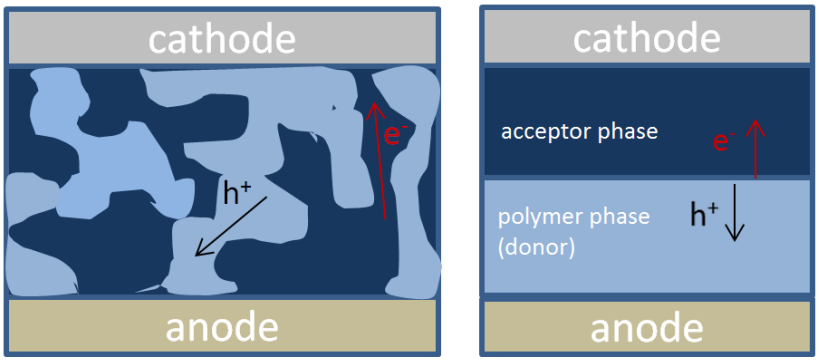

Figure 7: schematics of a bulk heterojunction (left) and a bilayer heterojunction (right) solar cell

The last layer is the cathode, it works as an electron collector. The most common cathode material is aluminium, however, silver is also used sometimes. The cathode is usually applied on top of the active layer via thermal evaporation.[16]

Figure 8 shows a typical device structure of a hybrid solar cell.

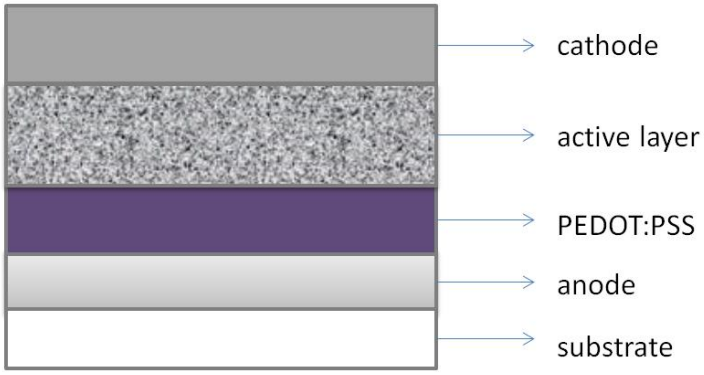

Figure 8: typical device architecture of a hybrid solar cell

The inverse assembly constitutes an alternative to the device architecture that is described above. In the inverted design, the charge carrier collection is opposite to the charge carrier collection in the conventional architecture. In this case, the electrode that is deposited on top of the device acts as a hole collector. Gold and

copper, materials that are commonly used for this purpose, have a high workfunction and are less air-sensitive. TiO_2 is often used as an electron collector, since it is transparent, stable and has a high electron mobility.[22]

1.8 Electrical Characteristics of Solar Cells

The electrical characteristics of a solar cell are determined by recording a current-voltage curve. Typically the voltage of the cell is varied through an applied load while the current is measured. Usually the cell is measured in two conditions, illuminated and dark. The data from both measurements are plotted. In Figure 9 the schematic I/V curves of a device under illumination (red line) and in the dark (blue line) are shown.

In order to make the results comparable, the light source is standardized. The standard used is air mass (AM) 1.5 global light intensity. AM 1.5 corresponds to the irradiance of the sun onto the earth surface at a solar zenith angle of 48.19°. Usually a power density of 1000 W/m² is used.[21]

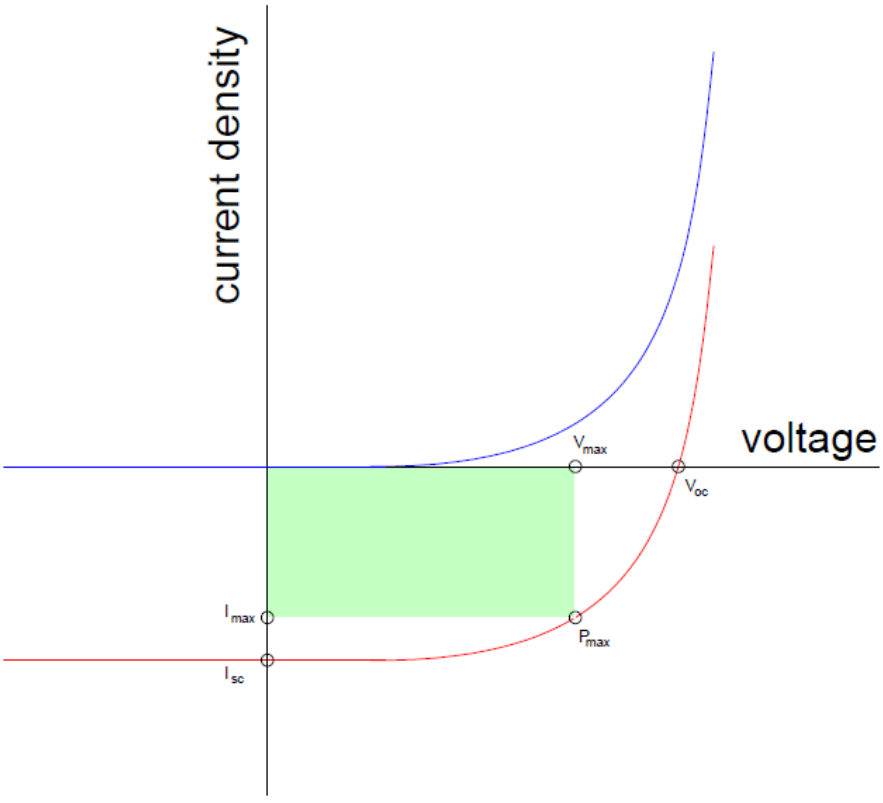

Figure 9: schematics of an I/V curve of a solar cell

The current that flows through the cell when there is no voltage applied is called the short circuit current (I_{SC}). The charge travels due to the internal potential difference which is equal to the open circuit voltage (V_{OC}). I_{SC} is dependent on the strength of illumination, thus, the above mentioned AM 1.5 standard is necessary in order to compare different solar cells.[20] I_{SC} is the maximal charge current that can be retrieved from the solar cell; it is influenced by the charge separation and transport efficiencies of the device and it scales with the area of the solar cell. Therefore, in order to compare the short circuit current of different cells, it is divided by the area of the device, yielding the short circuit current density (J_{SC}).[16,19]

The bias, at which the measured current in the cell is zero, is called the open circuit voltage (V_{OC}). It is the point where the applied voltage compensates the internal potential of the device. V_{OC} represents the maximum voltage difference that can be achieved between the two electrodes. It depends on the HOMO level of the donor and the CB level of the acceptor material. Furthermore, V_{OC} is constrained by the discrepancy in workfunctions of the used electrodes[20,23]

The point where the product of voltage and current is at its maximum is called the maximum power point, P_{max}.[12] The power conversion efficiency, PCE, represents the ratio between the electrical power output and the energy of the light that is absorbed by the solar cell (see equation 1).[1]

Equation 1: power conversion efficiency

$$PCE = \frac{P_{max}}{P_{in}} = \frac{V_{OC} * I_{SC} * FF}{P_{in}}$$

The fill factor (FF) defines the ratio between the product of current and voltage at the maximum power point and the product of open circuit voltage and short circuit current (see equation 2).[24] Thus, it describes the diode quality of the I/V curve. The diode quality of a bulk heterojunction solar cell depends on the nanomorphology of the active layer.[16]

Equation 2: fill factor

$$FF = \frac{P_{max}}{V_{OC} * I_{SC}} = \frac{V_{MPP} * I_{MPP}}{V_{OC} * I_{SC}}$$

The external quantum efficiency (EQE) is another important parameter of a solar cell. It represents the ratio between the collected electrons and the incident photons. In equation 3, EQE is described in two ways, where η_{abs}, η_{diff}, η_{diss}, η_{tr} and η_{cc} represent the efficiencies of the absorption, diffusion, dissociation, charge carrier transport and charge collection step, respectively.[16,20]

Equation 3: external quantum efficiency

$$EQE = \frac{1240 * I_{SC}}{\lambda * P_{in}} = \eta_{abs} * \eta_{diff} * \eta_{diss} * \eta_{tr} * \eta_{cc}$$

1.9 Preparation Methods of Nanoparticles for Use in Solar Cells

Next to the investigation of various material combinations for hybrid solar cells, there is also a lot of research being conducted on different synthetic routes towards hybrid materials for use in solar cells. Controlling the reaction process for each route is of uttermost importance because the PCE is severely influenced by impurities, such as capping agents, byproducts and surface defects, in the active layer.[2]

Basically, the synthetic routes can be divided into 3 groups: The classical approach, the infiltration approach and the in situ approach.[2]

The classical approach is the approach that is used most often. In this method, the first step is the colloidal nanoparticle synthesis, often followed by purification and a ligand exchange step. Subsequently, the nanoparticles are dissolved together with the polymer yielding the solution for the active layer of the solar cells. The capping agent plays an important part in the nanoparticle synthesis. Its role is to prevent particle agglomeration and to control growth and shape of the particles. Through the capping agent, it is possible to achieve a narrow size distribution and adjustable size and shape. However, the long chained molecules that function as capping agents have the negative side effect of representing a barrier for charge dissociation as well

as charge transport in the solar cell. This is why ligand exchange is crucial in order to achieve a good PCE in the resulting solar cells. In this step, ligands, such as long chained amines, bulky phosphines or phosphine oxides, are exchanged by shorter molecules such as pyridine, “smaller” amines or thiols. However, by using smaller molecules as capping agents, the solubility of the nanocrystals is reduced. In an alteration of the classical approach, that has been introduced recently, the ligand exchange is conducted in solid state after the active layer has been coated onto the substrate. This has the advantage, that it is possible to use shorter ligands without having solubility problems and thus, further improving the charge transport in the solar cell.[2,15,25]

In the infiltration approach porous or mesoporous inorganic structures are formed on one electrode and are subsequently filled with the organic polymer. Since the inorganic structure is connected directly to one electrode, there are no dead ends that inhibit charge transport. In this approach no ligands are required, thus, the ligand exchange step that often causes problems is avoided. The resulting structures are highly ordered and ligand free. It is not possible to achieve both these criteria with the classical or with the in situ approach. However, the preparation of the porous inorganic structure usually requires complicated process steps, high temperatures and long reaction times. Thus, the future prospects for this method are limited.[2,15]

In the in situ approach, the nanoparticles are synthesized directly in the active layer solution. The solution containing the polymer and the nanoparticle precursors is deposited onto the device. Subsequently the preparation of the active layer is finalized by a thermal annealing step in which the precursors decompose into the inorganic electron acceptors. The advantage of this step is that ligands are not necessary, thus the distance between nanoparticles and polymer is shorter leading to a better charge transport. On the other hand, the temperature at which the preparation of the nanoparticles can take place is limited since the reaction is being conducted in presence of the organic polymer. If the reaction temperature is too high, the structure and the optoelectrical properties of the polymer are lost. Furthermore, the shape and size of the nanocrystals is not as easily controlled as in the classical approach. Finally, there might be a higher defect density in the structure of the nanomaterial and the material might have a lower crystallinity resulting in worse electronic properties of the inorganic particles.[2,15,26,27]

1.10 Copper Indium Disulfide Nanoparticles

The properties of nanomaterials are tunable. In contrast to bulk materials, where the band gap is a constant that is specific for the material, the band gap of nanomaterials is size-dependent. This makes nanocrystals appealing materials for application in solar energy conversion or lighting display technology. Cadmium chalcogenide nanocrystals have exceptional optical properties they are already used in displays. However, the application of the most studied II-VI and IV-VI semiconductors is restricted because they contain the toxic materials cadmium and lead (e.g.: CdSe, CdTe, CdS, PbSe). There are some ternary semiconductors that have comparable optical properties while being less toxic. Examples for these alternatives are $CuInS_2$, $CuInSe_2$, $AgInS_2$ and $CuFeS_2$.[28,29,30]

Copper indium disulfide (CIS) is a direct semiconductor that is not toxic and has a high absorption coefficient of about 10^{-5} cm^{-1} in the visible range.[31] CIS has a bulk energy band gap of 1.53 eV. It has been calculated, that the band gap of chalcopyrite structured CIS nanocrystals can be tuned from 3.3 to 1.7 eV by changing the particle size from 1 to 6 nm.[32] The band gap of CIS nanocrystals can be varied not only through the size, but also through the copper to indium molar ratio.[33] Due to these properties, CIS is a suitable material for bioimaging, photocatalysis, light-emitting diodes and solar energy conversion.[28] The use of CIS in solar cells was first investigated by Arici et al. in 2003.[31]

Since the application of CIS nanoparticles in organic inorganic hybrid solar cells was first investigated, a lot of research has already been performed on this subject. Krause et al.[34] synthesized CIS via a colloidal method before introducing them into solar cells. They prepared devices with efficiencies of 0.05% using a P3HT / CIS system. Rath et al.[2] achieved efficiencies of up to 2.8% with PSiF-DBT / CIS solar cells using the in situ nanoparticle preparation method.

Bulk CIS crystallizes in chalcopyrite phase at room temperature. However, CIS nanocrystals can be synthesized in chalcopyrite, zincblende or wurzite structure. CIS nanocrystals can be prepared in diverse morphologies. Amongst others, nanopyramids, nanoplates, nanorods, spherical nanoparticles and nanowires have been reported. The crystallographic structure and shape of the resulting nanocrystals

are influenced by parameters such as the starting materials, ligands and solvents as well as reaction time and temperature.[28,35]

1.11 Ligand Exchange

As mentioned above, the use of inorganic materials as acceptors in hybrid solar cells provides many advantages such as enhanced absorption and conductivity. However, there are also some severe challenges that come with the use of these materials. Even though the inorganic semiconductors have a great intrinsic conductivity, the overall mobility of electrons in the composite material is low. The organic ligand that is bonded to the nanoparticle surface during the preparation process in order to control size and shape of the nanomaterial and enhance particle stability is an electrical insulator. It deters the charge transfer between donor and acceptor as well as the mobility of the electrons that are travelling through the acceptor material. However, it is difficult to completely remove the original ligand shell. Additionally, the unprotected particles are often insoluble and tend to aggregate. Furthermore, the surface of the particles without ligands exhibits defects that can act as charge carrier traps. Therefore, the preferred method is a ligand exchange with small molecules, which stop aggregation and minimize surface defects whereas allowing for charge transport.[16] Figure 10 shows the schematics of a nanoparticle capped with a ligand and without ligand.

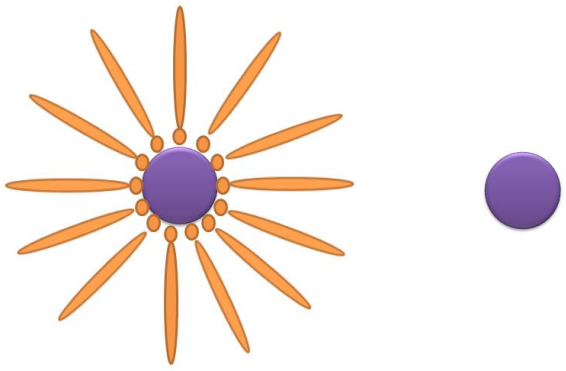

Figure 10: schematics of a nanoparticle with capper coordinated to the surface (left) and without capping agent (right)

Ligand exchange with pyridine has been widely investigated. Furthermore, short chained amines such as, for example butylamine or thiols such as t-butylthiol, have been explored as cappers.[2]

Recently ligand exchange with “smart” ligands was introduced. In this approach, the molecules used for ligand exchange consist of chains that are thermally cleavable in order to remove parts of the capper sphere. Alternatively, they contain conjugated groups to improve charge transfer. The down side of this type of ligands is the necessity of the extensive synthesis of the capping agents.[2]

Some other approaches have also been explored in addition to ligand exchange, such as for example a simple washing treatment with hexanoic acid in order to remove excess ligand molecules. The treatment with hexanoic acid results in salt formation and reduction of the ligand sphere.[36]

2 Experimental

2.1 Synthesis of Copper Indium Disulfide Nanoparticles

2.1.1 Colloidal Method using Oleic Acid and 1-Dodecanethiol

CIS nanoparticles were synthesized by a method published by Chen B, Zhong H, Zhang W, et al.[37]

For the synthesis 1 mmol (190 mg, 1 eq) CuI and 1 mmol (292 mg, 1 eq) $In(OAc)_3$ were mixed with 1 ml (4.2 eq) 1-dodecanethiol (1-DDT) and 10 ml octadecene (ODE) under N_2 atmosphere in a three-necked flask. The reaction mixture was heated to 120°C and degassed for 20 minutes. Subsequently, 0.5 ml (1.6 eq) of oleic acid (OA) was added and the reaction mixture was degassed for another 20 minutes. Afterwards, the flask was purged with nitrogen for 20 minutes and finally heated to 210 °C. After reaching 210 °C the reaction was stopped or alternatively, left to react for another hour.

The reaction mixture was left to cool down to room temperature. The nanoparticles were precipitated in excess acetone, centrifuged at 3660 rpm for 5 minutes and redissolved in toluene. This process was repeated up to 14 times.

Alterations in reaction time and in the amount of precursors used

- 76 mg (0.4 mmol, 1eq) CuI, 464 mg (1.6 mmol, 4 eq) $In(OAc)_3$, 0.5 ml (4 eq) OA and 1 ml (10.5 eq) 1-DDT, the reaction was stopped after the reaction temperature reached 210 °C
- 76 mg (0.4 mmol, 1eq) CuI, 198 mg (0.68 mmol, 1.7 eq) $In(OAc)_3$, 0.5 ml (4 eq) OA and 1 ml (10.5 eq) 1-DDT, the solvent ODE was purged with nitrogen before the synthesis, the reaction was stopped after the reaction temperature reached 210 °C
- 76 mg (0.4 mmol, 1eq) CuI, 198 mg (0.68 mmol, 1.7 eq) $In(OAc)_3$, 0.5 ml (4 eq) OA and 1 ml (10.5 eq) 1-DDT, the reaction was stopped one hour after the reaction temperature reached 210 °C
- 76 mg (0.4 mmol, 1eq) CuI, 198 mg (0.68 mmol, 1.7 eq) $In(OAc)_3$, 0.333 ml (2.7 eq) OA and 1 ml (10.5 eq) 1-DDT, the reaction was stopped one hour after the reaction temperature reached 210 °C

- 76 mg (0.4 mmol, 1eq) CuI, 198 mg (0.68 mmol, 1.7 eq) $In(OAc)_3$, no OA and 2 ml (21 eq) 1-DDT, the reaction was stopped one hour after the reaction temperature reached 210 °C
- 76 mg (0.4 mmol, 1 eq) CuI, 198 mg (0.68 mmol, 1.7 eq) $In(OAc)_3$, 0.5 ml (4 eq) OA and 0.357 ml (3.75 eq) 1-DDT, the reaction was stopped one hour after the reaction temperature reached 210 °C
- 76 mg (0.4 mmol, 1 eq) CuI, 198 mg (0.68 mmol, 1.7 eq) $In(OAc)_3$, 0.5 ml (4 eq) OA and 0.400 ml (4.3 eq) 1-DDT, the reaction was stopped one hour after the reaction temperature reached 210 °C
- 76 mg (0.4 mmol, 1 eq) CuI, 198 mg (0.68 mmol, 1.7 eq) $In(OAc)_3$, 0.5 ml (4 eq) OA and 0.460 ml (4.8 eq) 1-DDT, the reaction was stopped one hour after the reaction temperature reached 210 °C
- 76 mg (0.4 mmol, 1 eq) CuI, 198 mg (0.68 mmol, 1.7 eq) $In(OAc)_3$, 0.5 ml (4 eq) OA and 0.700 ml (7.3 eq) 1-DDT, the reaction was stopped one hour after the reaction temperature reached 210 °C
- 76 mg (0.4 mmol, 1 eq) CuI, 198 mg (0.68 mmol, 1.7 eq) $In(OAc)_3$, 0.5 ml (4 eq) OA and 0.600 ml (6.3 eq) 1-DDT, the reaction was stopped one hour after the reaction temperature reached 210 °C
- 76 mg (0.4 mmol, 1 eq) CuI, 198 mg (0.68 mmol, 1.7 eq) $In(OAc)_3$, 0.5 ml (4 eq) OA and 0.500 ml (5.2 eq) 1-DDT, the reaction was stopped one hour after the reaction temperature reached 210 °C
- 190 mg (1 mmol, 1 eq) CuI, 292 mg (1 mmol, 1 eq) $In(OAc)_3$, 0.5 ml (1.6 eq) OA and 1 ml (4.2 eq) 1-DDT, the reaction was stopped one hour after the reaction temperature reached 210 °C
- 141 mg (0.74 mmol, 1 eq) CuI, 368 mg (1.26 mmol, 1.7 eq) $In(OAc)_3$, 0.5 ml (2.1 eq) OA and 1 ml (5.7 eq) 1-DDT, the reaction was stopped one hour after the reaction temperature reached 210 °C

Different precipitants that were used

The reaction product of the synthesis, where 76 mg (0.4 mmol, 1eq) CuI, 198 mg (0.68 mmol, 1.7 eq) $In(OAc)_3$, 0.5 ml (4 eq) OA and 1 ml (10.5 eq) 1-DDT were used and the reaction was stopped after the reaction temperature reached 210 °C, was precipitated using the following different precipitating agents.

- Acetone
- Ethanol
- Methanol
- Ethanol : Hexane 1 : 1

2.1.2 Hot Injection Method using Oleic Acid and Hexamethyldisilathiane

The nanoparticles were prepared using a variation of the method published by Hines and Scholes.[38]

For the synthesis 0.4 mmol (68 mg, 1 eq) $CuCl_2*2H_2O$, 0.68 mmol (150 mg, 1.7 eq) $InCl_3$ and 1 ml (8 eq) OA were mixed with 10 ml ODE under N_2 atmosphere in a three-necked flask. Subsequently, the reaction mixture was heated to 120 °C. After reaching 120 °C the flask was degassed and it was further heated to 150 °C for about an hour until everything was dissolved.

0.54 mmol (1.35 eq) hexamethyldisilathiane (HMDS) were dissolved in 6 ml ODE and purged with nitrogen for 5 minutes. Subsequently, the prepared sulfur source was injected into the reaction solution. After 5 minutes the reaction was quenched with cold acetone. Finally, the resulting nanoparticles were precipitated in acetone and redispersed in toluene.

<u>Different precursors and precursor amounts that were used in the reaction</u>

- 189 mg (0.68 mmol, 1.7 eq)) In_2O_3 , 58 mg (0.4 mmol, 1 eq) Cu_2O, 0.682 ml (2.2 eq) OA
- 188 mg (0.68 mmol, 1.7 eq) In_2O_3 , 33 mg (0.4 mmol, 1 eq) CuO, 0.823 ml (2.6 eq) OA
- 150 mg (0.68 mmol, 1.7 eq) $InCl_3$, 68 mg (0.4 mmol, 1 eq) $CuCl_2*2H_2O$, 0.823 ml OA
- 150 mg (0.68 mmol, 1.7 eq) $InCl_3$, 68 mg (0.4 mmol, 1 eq) $CuCl_2*2H_2O$, 1.5 ml (2.6 eq) OA
- 150 mg (0.68 mmol, 1.7 eq) $InCl_3$, 40 mg (0.4 mmol, 1 eq) CuCl, 1 ml (8 eq) OA
- 150 mg (0.68 mmol, 1.7 eq) $InCl_3$, 40 mg (0.4 mmol, 1 eq) CuCl, 10 ml (80 eq) OA

- 150 mg (0.68 mmol, 1.7 eq) $InCl_3$, 40 mg (0.4 mmol, 1 eq) CuCl, 1 ml (7.6 eq) Oleylamine (OLAM) 70%

Variations in the reaction time

- The reaction that was performed using copper and indium chlorides was conducted with reaction times of 3 and 5 minutes.

2.1.3 Colloidal Method using Oleylamine and Dodecanethiol

The nanocrystal preparation was conducted after a method published by Krause C, Miranti R, Witt F, et al.[34]

For the synthesis 1 mmol (292 mg, 4 eq) $In(OAc)_3$, 1 mmol (123 mg, 4 eq) Cu(OAc) and 1 mmol (387 mg, 4 eq) trioctylphosphine oxide (TOPO) were mixed with 10 ml OLAM 70% in a three-necked flask in nitrogen atmosphere. The reaction mixture was degassed for 20 minutes. Afterwards, it was purged with nitrogen and heated to 240 °C. At around 200 °C, when the colour of the solution turned to brown, a combination of 0.25 mmol (58.8 µl, 1 eq) t-DDT and 0.5 mmol (119.8 µl, 2 eq) 1-DDT was added. The mixture was left to react at 240 °C for 1 hour.

Finally, after the solution had cooled down to room temperature, the particles were precipitated in ethanol and redissolved in chlorobenzene (CB). This process was repeated 3 times.

The same reaction was also performed using 116 mg (0.95 mmol, 3.8 eq) Cu(OAc), 307 mg (1.05 mmol, 4.2 eq) $In(OAc)_3$ and 10 ml of OLAM 80-90%.

2.2 Preparation of Solar Cells

2.2.1 Bulk Heterojunction Assembly

ITO covered glass substrates were sonicated for 10 minutes at 40°C in an ultrasonic bath and stored in isopropanol. Subsequently, the devices were removed from the isopropanol bath and dried with lint-free cloths. The remaining dust was removed with a stream of nitrogen gas and the conductive side was determined with a multimeter. Afterwards, the surface of the substrate was activated using plasma etching. Next, the devices were coated with PEDOT:PSS for bulk heterojunction solar cells (Clevios PVP. Al 4083) via spin coating at 2500 rpm for 30 seconds, with an acceleration of 300 rpm/s. The PEDOT:PSS covered substrates were then transferred into the glove box and tempered for 10 minutes at 150 °C. Afterwards, the active layer was applied on top of the PEDOT:PSS layer through doctor blading with a wet film thickness of 100 µm using 30 µl solution. The velocity of the doctor blading, as well as the temperature at which the active layer was deposited, were varied (see table 1). Finally, 200 nm of Al electrodes were applied at a pressure of around $1*10^{-5}$ mbar, using evaporation deposition. The devices were characterized by I/V measurements. Figure 11 shows a schematic composition of the solar cells that were prepared as described above.

Table 1: doctor blading parameters of the active layer deposition that were varied for the bulk heterojunction assembly

temperature	velocity of doctor blading [mm/s]		
40 °C	10	12.5	15
room temperature	10	-	15

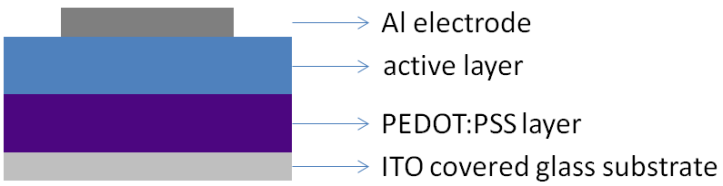

Figure 11: composition of a bulk heterojunction assembly

2.2.2 Inverse Bulk Heterojunction Assembly

ITO covered glass substrates were sonicated in an ultrasonic bath for 10 minutes at 40 °C and stored in isopropanol. Afterwards, the devices were removed from the isopropanol bath and dried with lint-free cloths. The dust was removed with a nitrogen stream. Subsequently, the conductive side was determined with a multimeter and the surface of the substrates was activated by plasma etching. The devices were coated with a 0.1 M solution of titaniumdiisopropoxid bisacetyl acetonate via doctorblading. For this purpose, 30 µl of the solution were applied onto the devices with a wet film thickness of 100 µm and a velocity of 25 mm/s at a temperature of 40 °C. Afterwards, the coated glass slides were put on a ceramic heating plate at around 400 °C for 30 minutes. Subsequently, the surface was activated again by plasma etching. Then, the devices were transferred into the glove box, where the active layer was applied via doctor blading with a wet film thickness of 100 µm using 30 µl of the solution. The velocity and the temperature, at which the doctor blading process was conducted, were varied (see table 2). Afterwards, a layer of PEDOT:PSS was added onto the devices outside of the glove box. The PEDOT:PSS layer was doctorbladed onto the devices at a temperature of 60 °C, with a wet film thickness of 100 µm, at a velocity of 15 mm/s. For this purpose, 50 µl of PEDOT:PSS solutions for inverse bulk heterojunction solar cells (Clevios HTL Solar) that was diluted with water with a ratio of 1:1 were used. The devices were transferred back into the glove box, where 120 nm of Ag electrodes were applied at a pressure of $1*10^{-5}$ mbar via evaporation deposition. Finally, the cells were characterized through I/V measurements. Figure 12 shows the composition of the solar devices that were prepared as described above.

Table 2: varied doctor blading parameters of the active layer deposition for the inverse bulk heterojunction assembly

temperature	velocity of doctor blading [mm/s]	
40 °C	10	15
35 °C	10	15

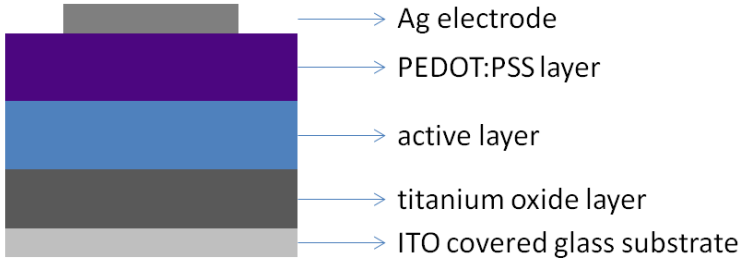

Figure 12: composition of an inverse bulk heterojunction assembly

The devices that were built using the inverse bulk heterojunction assembly were all prepared using CIS with a copper to indium molar ratio of 1 : 1.7. The active layer solution for the inverse bulk heterojunction assembly was prepared with a polymer to inorganic weight ratio of 1 : 7.

2.2.3 Preparation of the Active Layer

5 mg/ml solutions of the polymer poly[2,7-(9,9-dioctyl-dibenzosilole)-alt-4,7-bis(thiophen-2yl)benzo-2,1,3-thiadiazole] (PSIF-DBT) in chlorobenzene and chloroform respectively was prepared and stirred at room temperature for at least one hour. Subsequently, the previously synthesized CIS nanoparticles were dissolved in the polymer solution. The polymer to CIS weight ratio was varied as can be seen in table 3. Solutions were also diluted with various amounts of the respective solvent (see table 3). The active layer solution was left to stir between 10 and 20 minutes before it was applied onto the devices, as described above.

Table 3: different polymer to CIS weight ratios and different volume ratios of dilution that were used in the active layer preparation

polymer to CIS weight ratios	volume ratios of dilution of active layer solutions with solvent
1 : 15	not diluted 1 : 0.5 1 : 1 1 : 3 1 : 7 1 : 11
1 : 9	not diluted 1 : 0.5
1 : 7	not diluted 1 : 0.5
1 : 5	not diluted 1 : 0.5
1 : 3	not diluted

2.3 Ligand Exchange

2.3.1 Ligand Exchange with Pyridine

2.3.1.1 Pyridine Ligand Exchange in Solution

The CIS nanoparticles that were prepared as described in chapter 2.1.1 were dissolved in pyridine. The amounts of CIS and pyridine used for the reactions are listed in table 4. The reaction was conducted under nitrogen atmosphere at 90 °C for 15 hours. Subsequently, the nanoparticles were precipitated in a mixture of acetone and ethanol with a volume ratio of 1 : 1. Afterwards, they were dissolved in toluene and precipitated a second time. Finally, the resulting pyridine capped nanoparticles were dried under vacuum overnight.

Table 4: amount of CIS and pyridine that were used for the ligand exchange procedure

CIS [mg]	pyridine [ml]
153	1
147	3
86	3
276	4
186	4

2.3.1.2 Pyridine Ligand Exchange in Solid State

Alternatively, a ligand exchange with pyridine was conducted after the deposition of the active layer. For this purpose, the device on which the active layer had been deposited, as described above, was soaked in pyridine for 30 seconds, followed by spin coating at 2200 rpm for 25 seconds. Subsequently, the device was soaked in acetonitrile for 20 seconds and spin-coated for 20 seconds at 2200 rpm. Finally, the cell was soaked in n-hexane for 20 seconds and spin-coated for another 20 seconds at 2200 rpm. After this ligand exchange the next layer was applied to the device as described previously.

2.3.2 Ligand Exchange with Butylamine

279 mg of the CIS nanoparticles that were prepared as described in chapter 2.1.1 were dissolved in 2 ml butylamine. The ligand exchange with butylamine was conducted under nitrogen atmosphere at a temperature of 75 °C for 15 hours. The butylamine capped particles were then precipitated with a mixture of acetone and ethanol and dried under vacuum for 2 hours.

2.3.3 Ligand Exchange with 1,2-Ethanedithiol

The ligand exchange with 1,2-ethanedithiol was performed in solid state after the deposition of the active layer. For this purpose, 3 ml of a 0.01 M 1,2-etanedithiol solution in acetonitrile was prepared and the device was soaked in this solution for 30 seconds before spin-coating at 2200 rpm for 25 seconds. Afterwards, the coated slide was bathed in 3 ml acetonitrile for 20 seconds and spin-coated for 20 seconds at 2200 rpm. Finally, the device was soaked in 1 ml n-hexane for 20 seconds and spin-coated at 2200 rpm for 20 seconds. This ligand exchange was followed by the next deposition step as described above.

2.4 Characterization

2.4.1 Measurement of the I/V Characteristics

After the preparation of the solar cells, I/V characteristics were measured. For this purpose, the devices were put in a custom-made box in the glove box, through which the electrical contacts to a Keithley 2400 source measurement unit were provided. The box also contained a photo diode to measure the light intensity. The solar cells were measured twice, once in the dark and once under an illumination of 1000 W/m². The spectral mismatch was not corrected. The light was generated by a tungsten halogen lamp. The source measurement was connected to a computer and the measurement was conducted automatically by a Labview program. During the measurement the voltage was changed from 1.5 V to -0.5 V with a step width of 0.01 V.

2.4.2 Determination of the Layer Thickness

The thickness of the layer of the produced solar cells, as well as the roughness was determined with a Bruker Dektak XT profilometer. For the purpose of assessing the active layer thickness, a scratch was made into the film. Subsequently, the profile of the surface of the scrape and its surroundings was measured. The step height between the active layer and the scratch constituted the film thickness. Usually, the thickness and roughness of a device were measured on three different positions in order to obtain more accurate results.

2.4.3 UV/VIS Measurements

The absorption of active layers with different compositions was measured between 300 nm and 1000 nm using a Shimadzu UV 1800 and a PerkinElmer Lambda 35 UV/VIS Spectrometer.

For the measurements 300 µl of solutions containing various CIS concentrations and 5 mg/ml of the polymer PSiF-DBT in CB were prepared and stirred for about 15 minutes. Subsequently, the surface of glass substrates with a size of about 2.5 cm x 2.5 cm was activated via plasma etching. Finally, the active layer solutions were spin-coated onto the glass substrate for 30 seconds at 4500 rpm and measured as described above. In table 5 the solutions that were measured with UV/VIS, are summarized.

Table 5: summary of solutions that were measured with UV/VIS

type of CIS	polymer : CIS weight ratio			
no ligand exchange	only polymer	1:5	1:9	1:15
pyridine capped	only polymer	1:5	1:9	1:15

2.4.4 Photoluminescence Quenching Experiments

In order to determine the photoluminescence quenching of the PSiF-DBT / CIS system, the samples that had been prepared as described in chapter 2.4.3 were also measured with a Hitachi F-7000 fluorescence spectrophotometer. For these experiments an excitation wavelength of 590 nm was used. The measurement was started at a wavelength of 610 nm and ended at a wavelength of 900 nm. The analysis was performed using a slit width of 2.5 nm and a voltage of 750 V.

2.4.5 X-ray Diffraction Measurements

The prepared CIS nanoparticles were analyzed using X-ray diffraction (XRD). The measurements were conducted using the diffractometers Siemens D501 and Bruker D8 Advance with a copper tube at 40 kV and 30 mA. The measurement setup that was used was the Bragg-Brentano geometry. The x-ray diffraction measurements were performed by Birgit Kunert and Ao. Univ.-Prof. Dipl.-Ing. Dr. techn. Franz-Andreas Mautner.

2.4.6 Thermo-Gravimetric Analysis

Thermo-gravimetric analysis of the prepared CIS nanoparticles was conducted with a Netzsch Jupiter 449 C simultaneous thermal analyzer. The measurements were performed under helium atmosphere at a heating rate of 10 °C/min. The samples were measured between 20 °C and 550 °C. The analysis was performed by Amtsrätin Ing. Josefine Hobisch.

2.4.7 Infrared Spectroscopy

The capping agent of the CIS nanoparticles was analyzed with FT-IR spectroscopy. FT-IR spectra of CIS nanoparticles as well as pure oleic acid were recorded with a Bruker, ALPHA FT-IR spectrometer between wavenumbers of 4000 cm^{-1} and 400 cm^{-1}.

2.4.8 Transmission Electron Spectroscopy and Energy Dispersive X-Ray Analysis

For the transmission electron microscopy (TEM) and the energy dispersive x-ray (EDX) analysis, samples, synthesized with a copper to indium ratios of 1 : 1 and 1 : 1.7, were dissolved in toluene at a concentration of 10 mg/ml. Further sample preparation and the TEM and EDX measurements were performed by DI Dr. Karin Wewerka at the Institute for Electron Microscopy and Nanoanalysis (FELMI) at Graz University of Technology.

3 Results and Discussion

3.1 Copper Indium Disulfide Nanoparticle Synthesis

The difference in chemical properties of the two cations results in a challenge for the synthesis of CIS nanocrystals. In^{3+} and Cu^{+} are hard and soft Lewis acids, respectively. Since sulfur compounds are usually soft Lewis bases, the formation of copper sulfides may be favored, if the reaction is not balanced. The reactivity of copper and indium can be adjusted by adding stabilizers, such as, for example a thiol and a carboxylic acid. Another way to solve the problem of the different reactivities is the utilization of precursors that contain both cations in one compound. Through the decomposition of this precursor, the same amount of copper and indium is set free. Thus, the formation of CIS is favored. For most preparation methods organic solvents are used. However, a few water-based procedures have been published as well. The synthesis or CIS nanoparticles can be conducted using various different metal salts and sulfur sources. Hot-injection and heating-up syntheses yield the best size and shape control.[28]

Oleylamine is one of the most common capping agents used for nanoparticle synthesis.[28,39] However, it binds strongly to the surface of the resulting nanocrystals. Therefore, the ligand exchange step is rather difficult. Another frequently used capping agent is oleic acid (OA).[28] It might be easier to remove OA from the surface of the synthesized nanoparticles with ligand exchange. Thus, in this work most of the syntheses were performed with OA.

In this chapter the results of the three different CIS nanoparticle syntheses that were performed during this thesis, are displayed and discussed.

3.1.1 CIS Synthesis Using Oleic Acid and 1-Dodecanethiol

CIS nanoparticles were synthesized by a method published by Zhong H. et al[37], using 4.2 mmol 1-dodecanethiol (1-DDT), a total of 1.08 mmol of copper and indium salt with a copper to indium molar ratio of 1 : 1.7, 10 ml octadecene (ODE) and 1.6 mmol OA (see chapter 2.1.1). The synthesis yielded CIS nanoparticles. This can be seen in the corresponding XRD pattern (figure 13). However, it led to the formation of an insoluble gel during the work up process. Since it was impossible to

extract the nanoparticles that were enclosed in the generated gel, the yield was extremely low.

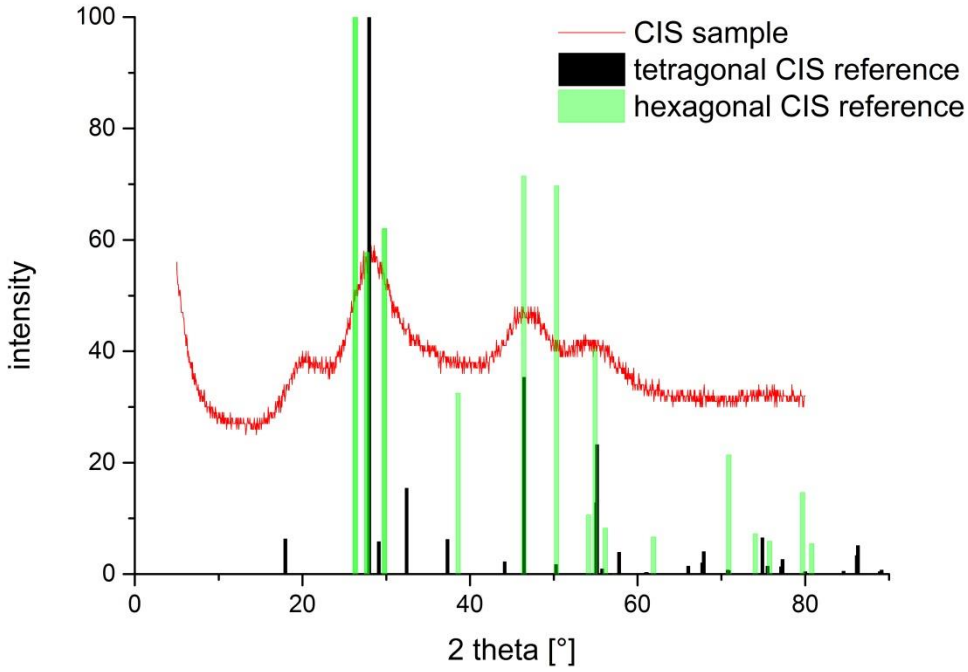

Figure 13: XRD pattern of CIS nanoparticles synthesized with 4.2 mmol 1-DDT

From the XRD pattern shown in figure 13 it can be derived that the synthesized CIS has a tetragonal body-centered crystal structure. The three main signals are at 28° (112), 46° (204) and 55° (312). The shoulders of the signal at 28° indicate that there might be a small fraction CIS with a hexagonal crystal structure present in the sample as well.

The size of the particles can be estimated from the XRD pattern using the Scherrer equation (see equation 4).

Equation 4: Scherrer equation

$$d = \frac{K * \lambda}{\Delta(2\theta) * \cos(\theta)}$$

d … diameter of the particles

K … shape factor, for spherical particles it is 0.9

λ … wavelength

2θ … scattering angle

The synthesized CIS nanoparticles had a diameter of approximately 2.0 nm.

3.1.1.1 Approaches for Preventing the Gel Formation

3.1.1.1.1 Use of Different Precipitants

The precipitation steps were carried out with acetone. It was assumed that some reaction takes place during the workup with acetone, yielding the gel. In order to prevent the formation of the gel, other precipitants were tried out. The use of methanol led to the formation of two phases and no precipitation took place. Furthermore, a 1 : 1 mixture of ethanol and hexane was used. Yet it was not possible to recover the product with this mixture. Ethanol alone did work as a precipitating agent. However, the gel developed despite the different precipitant. From these experiments it was concluded, that acetone was not the reason for the formation of the gel. Thus, for all further experiments the nanoparticles were precipitated with acetone.

3.1.1.1.2 Variation of the Reaction Time

Small particles have a very high surface to volume ratio. Therefore, they have a great surface area and thus are very reactive. In order to increase the size and consequently reduce the reactivity and maybe prevent the formation of the gel, the reaction time was increased. The experiment was done using two different reaction times. If a longer reaction time is used, the resulting nanoparticles are bigger. The particle size correlates with the broadness of the signal in the XRD pattern. Sharper signals indicate bigger particles. Figure 14 shows two XRD patterns of nanoparticles that were synthesized with different reaction times. It can be seen that the signals of the sample with shorter reaction time are broader.

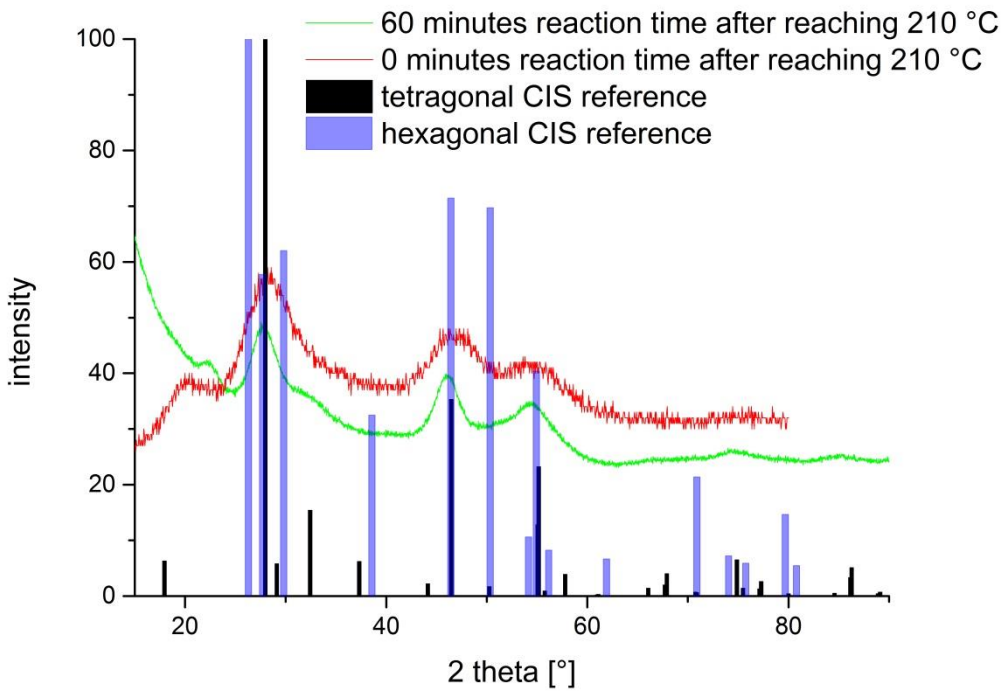

Figure 14: XRD pattern of synthesized CIS nanoparticles with different reaction time

The diameters of the nanoparticles were estimated using the Scherrer equation as explained above. The particles that were synthesized with a reaction time of 0 minutes after a temperature of 210 °C had been reached, had a diameter of approximately 2.1 nm. A reaction time of 60 minutes yielded nanocrystals with a diameter of around 3.8 nm.

3.1.1.1.3 Variation in the Amount of Capping Agent

Since it was assumed that the formation of the gel might be due to a reaction of OA with air, the solvent ODE was purged with nitrogen before it was introduced into the reaction flask. However, it did not have any effect on the formation of the gel.

OA as well as 1-DDT function as capping agents. Thus, it is possible to replace the OA with DDT and perform the reaction using only 1-DDT.[40,41,42] The reaction was performed using 8.4 mmol 1-DDT and a total of 1.08 mmol of copper and indium salt. Yet, the gel developed even faster than during the reactions that were conducted with OA.

This result led to the assumption that the amount of 1-DDT might have an influence on the gel formation. Therefore, the amount of 1-DDT used was reduced to 1.5 mmol while the total amount of salt was still 1.08 mmol. This time, no gel developed during the work-up process. However, the recorded XRD pattern showed that the product was not pure tetragonal copper indium disulfide. The corresponding XRD pattern is shown in figure 15.

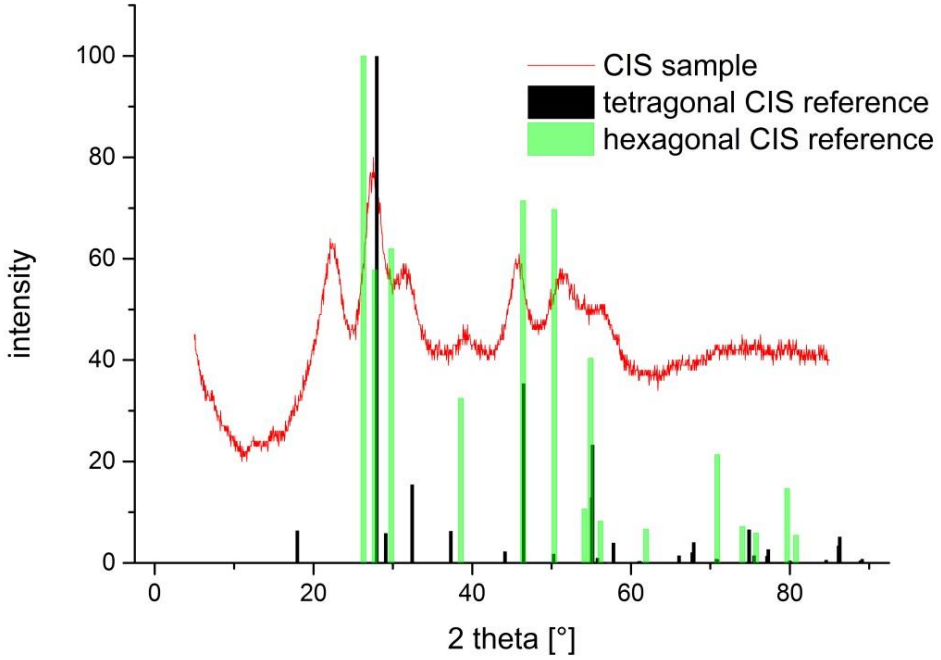

Figure 15: XRD pattern of the CIS nanoparticles synthesized with 1.5 mmol 1-DDT

The drastic reduction of the used amount 1-DDT results in the formation of an additional hexagonal CIS phase as can be seen in figure 15, from the signals at 39° and 50°. Furthermore, there is an additional signal at 20° that can neither be explained with the tetragonal CIS reference nor with the hexagonal CIS reference. This signal is probably due to the capping agent. Thus, the amount of 1-DDT was gradually increased, while the total amount of copper and indium salts was kept at 1.08 mmol. XRD pattern of CIS nanoparticles synthesized with 1.5 mmol, 1.7 mmol, 2.1 mmol and 4.2 mmol 1-DDT were recorded. The results are summarized in figure 16.

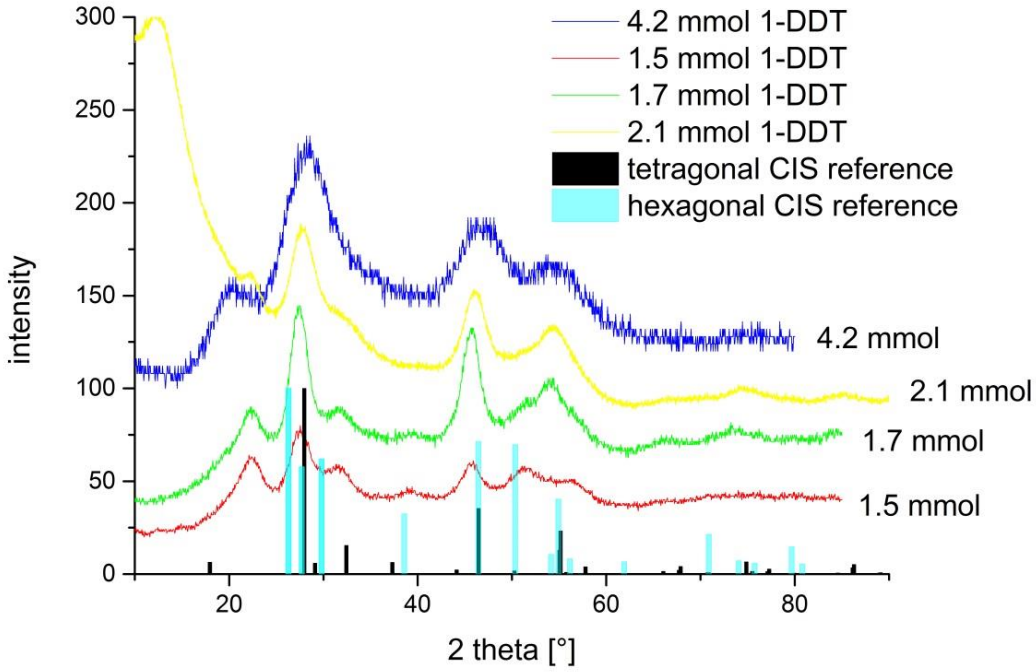

Figure 16: XRD patterns of CIS nanoparticles synthesized with different amounts of 1-DDT

As can be seen in figure 16, the signals at 39° and 50° gradually decrease with the amount of 1-DDT used in the synthesis. The patterns of the products where 4.2 and 2.1 mmol of 1-DDT were used for the synthesis show almost no signals at the above mentioned 2theta values. The signal at 20° probably varies due to the different amount of capping agent present in the samples.

As discussed above, the preparation of CIS nanoparticles with 4.2 mmol 1-DDT yielded a gel. The synthesis was also conducted with 2.5 mmol and 2.9 mmol 1-DDT. However, these experiments also produced a gel. Thus, 2.1 mmol 1-DDT seems to be the optimal amount for the preparation of tetragonal CIS nanoparticles, if a total amount of copper and indium salts of 1.08 mmol is used.

3.1.1.2 CIS Synthesis with Different Copper to Indium Molar Ratios

The synthesis was also conducted with a copper to indium molar ratio of 1 : 1, using the same amount of 1-DDT that was discovered to be the optimal value for the copper to indium molar ratio of 1 : 1.7. The resulting XRD pattern is shown in figure 17.

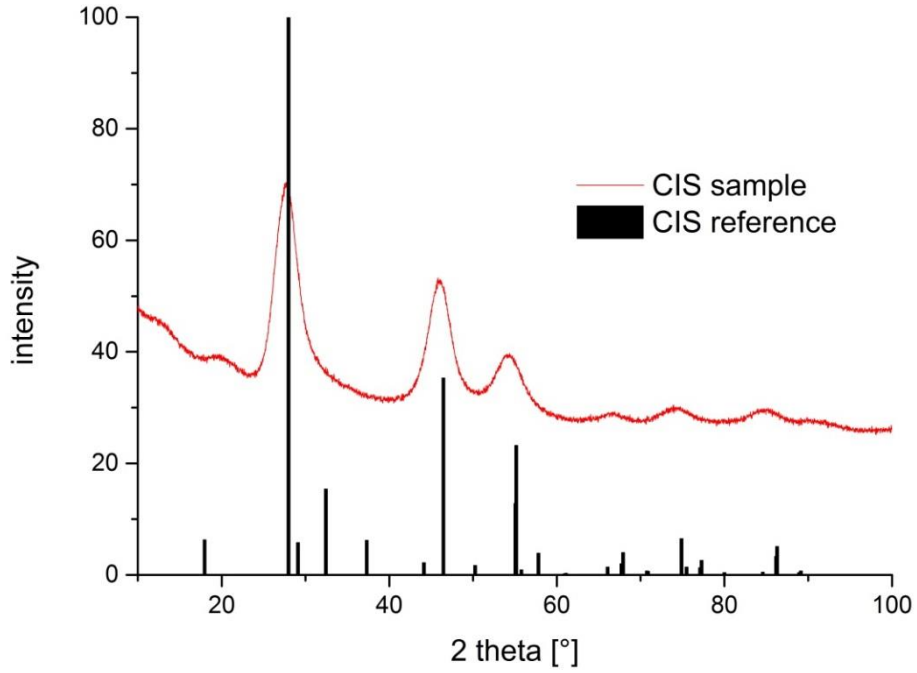

Figure 17: XRD pattern of CIS synthesized with a copper to indium molar ratio of 1 : 1

As can be seen in figure 17, the synthesis yielded the same tetragonal crystal structure despite the variation of the copper to indium molar ratio. The particle size was estimated using the Scherrer equation (equation 4). The particles had a diameter of approximately 3.2 nm.

3.1.1.3 Transmission Electron Microscopy

In order to further analyze the synthesized CIS nanoparticles, a transmission electron microscopy (TEM) analysis was performed. Two samples, synthesized with different copper to indium ratios, were analyzed. The TEM images of these samples are shown in figure 18 and figure 19.

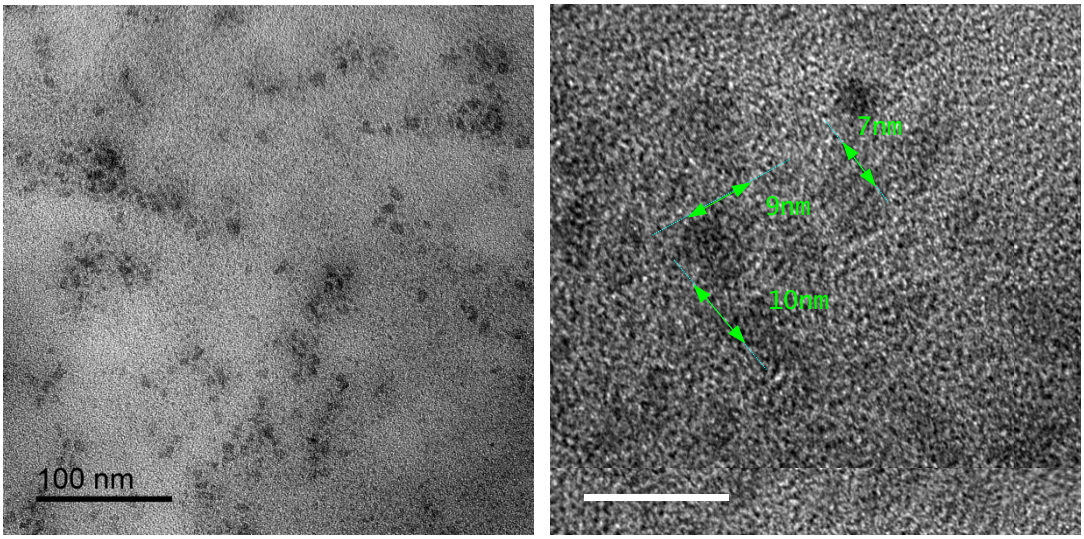

Figure 18: TEM images of CIS nanoparticles with a copper to indium ratio of 1 : 1.7

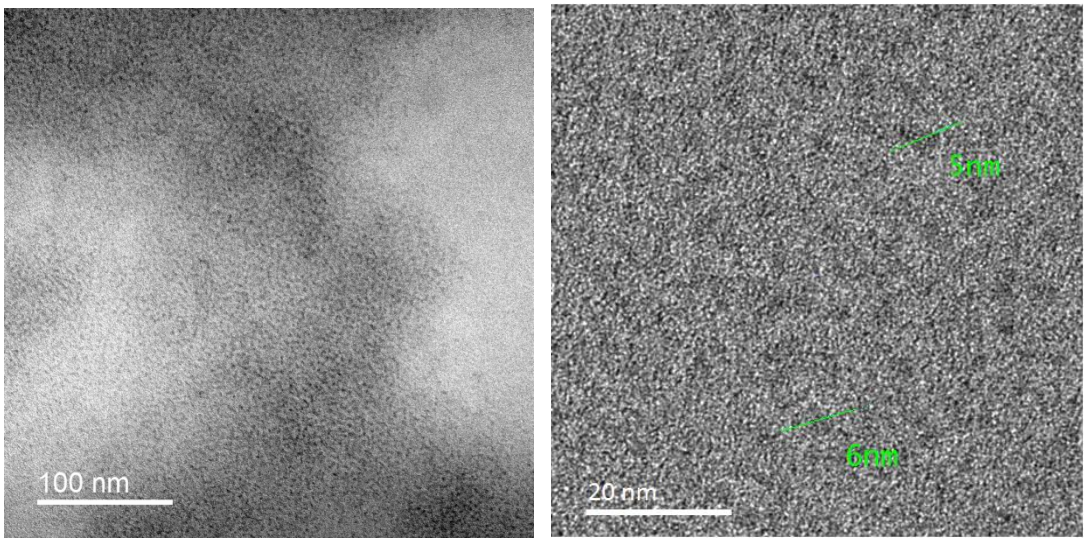

Figure 19: TEM images of CIS nanoparticles with a copper to indium ratio of 1 : 1

The TEM images show that the nanoparticles have a diameter between 5 and 10 nm. The syntheses using different copper to indium ratios yielded comparable particle sizes. The estimation from the XRD pattern, using the Scherrer equation (equation 4), yielded a smaller particle size of around 4 nm. Since the XRD analysis shows only the crystalline parts of the sample, amorphous part is not included in the particle size. On the other hand, the TEM analysis shows the whole sample (crystalline and amorphous part). Thus, the results show a bigger particle size.

3.1.1.4 Energy Dispersive X-Ray Spectroscopy

The two samples that were investigated with TEM were also examined with energy dispersive x-ray spectroscopy (EDX) in order to discover differences in the elemental composition between the samples. The EDX patterns of the samples are shown in figure 20.

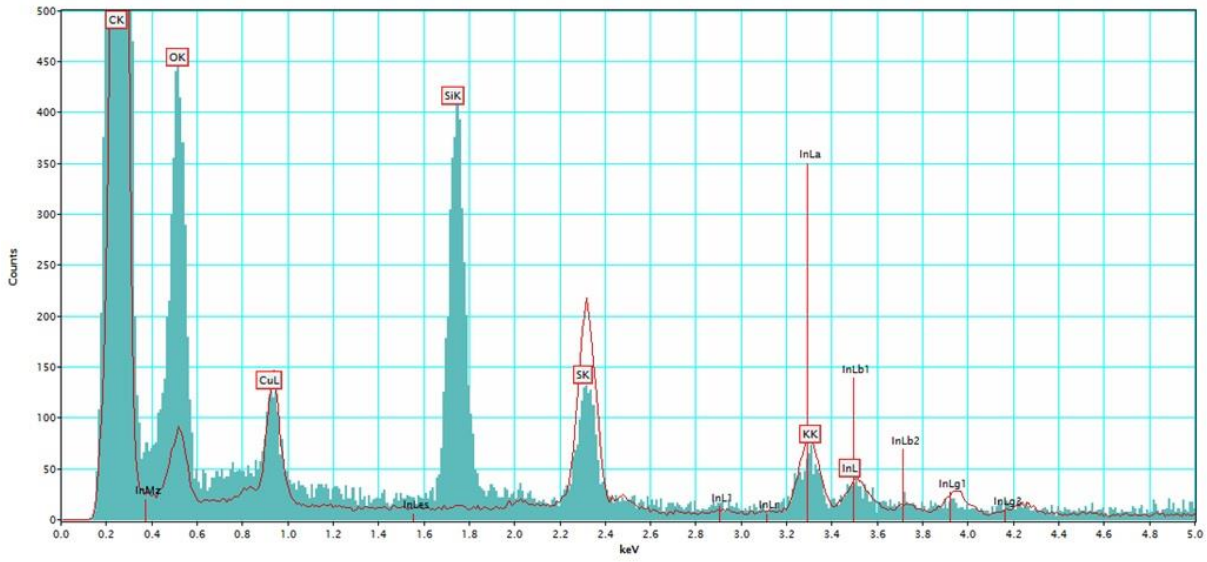

Figure 20: EDX pattern of CIS nanoparticles synthesized with a copper to indium ratio of 1 : 1 (red line) and 1 : 1.7 (blue graph) normed on the amount of indium in the sample

For the measurement, the samples were placed on a copper grid. Therefore, the amount of copper in the sample cannot be quantified. However, the relative amount of indium and sulfur in the samples can be compared. The sulfur signal of the sample with a copper to indium ratio of 1 : 1 is higher. Thus, this sample contains a smaller proportion of indium, which is consistent with the expected result, since less indium was introduced in the reaction.

Figure 20 also shows, that there is a silicon contamination in the sample with a copper to indium ratio of 1 : 1.7. Shortly before this sample has been synthesized, a synthesis with hexamethyldisilathiane had been performed. Therefore, it is suspected, that the silicon contamination originates from this previously used chemical.

3.1.1.5 Analysis of the Capping Agent and Ligand Exchange

3.1.1.5.1 IR Measurement

IR measurements were performed in order to characterize the ligand shell of the prepared nanocrystals. The results of the IR analysis of free oleic acid and of the CIS nanoparticles are shown in figure 21.

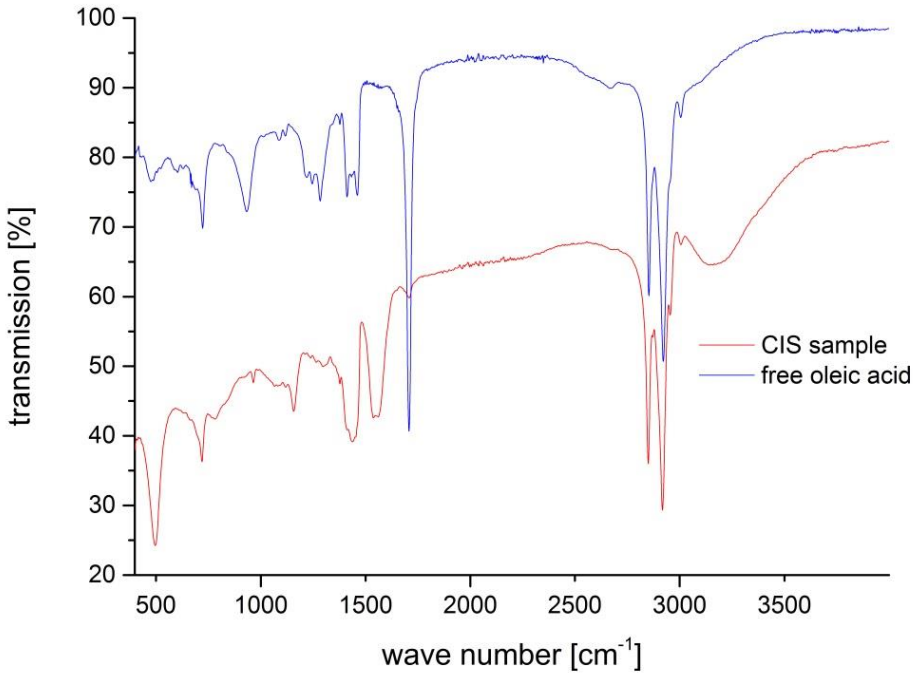

Figure 21: IR spectrum of oleic acid in CIS sample and free oleic acid

There is a C=O stretching vibration band of the carboxyl group in the spectrum of the free OA at 1705 cm^{-1}. There is no corresponding peak in the spectrum of the OA in the CIS sample. However, there are two bands at 1443 and 1555 cm^{-1} that indicate symmetric and asymmetric stretching vibration of COO^-. Thus, it is concluded that the OA is chemisorbed onto the CIS nanoparticles in form of a carboxylate, where the two oxygen atoms are coordinated symmetrically to the nanocrystals. There are two possible ways of adsorption of OA onto the metal surface. In a bidentate bond the two oxygen atoms are bound to the surface, while in the monodentate bond the hydrogen atom is replaced by the metal atom. If the OA was coordinated to the surface through a monodentate bond, the C=O stretching vibration at around 1700 cm^{-1} would still be present.[43]

The peaks of both recorded IR spectra are listed and interpreted in table 6.

Table 6: assignments of IR bands of free oleic acid and oleic acid adsorbed onto CIS nanoparticles

free oleic acid		
wave number [cm^{-1}]	vibrations	fragment
1705	C=O stretching vibration	COOH
2854	symmetric C-H stretching vibration	CH_2 acyclic chain
2922	asymmetric C-H stretching vibration	CH_2 acyclic chain
oleic acid adsorbed on CIS sample		
wave number [cm^{-1}]	vibrations	fragment
1443	symmetric COO^- stretching vibration	COO^-
1555	asymmetric COO^- stretching vibration	COO^-
2854	symmetric C-H stretching vibration	CH_2 acyclic chain
2922	asymmetric C-H stretching vibration	CH_2 acyclic chain
3150	O-H stretching vibration	COOH

3.1.1.5.2 STA Analysis

The CIS nanoparticles were analyzed using thermo-gravimetric analysis in order to determine the amount of capping agent present in the sample.

A sample was measured after a single precipitation step as well as after four precipitation steps. Subsequently, ligand exchange with pyridine was performed. Ligand exchanged samples were analyzed after one precipitation step as well as after two precipitation steps. The results of those four measurements are shown in figure 22.

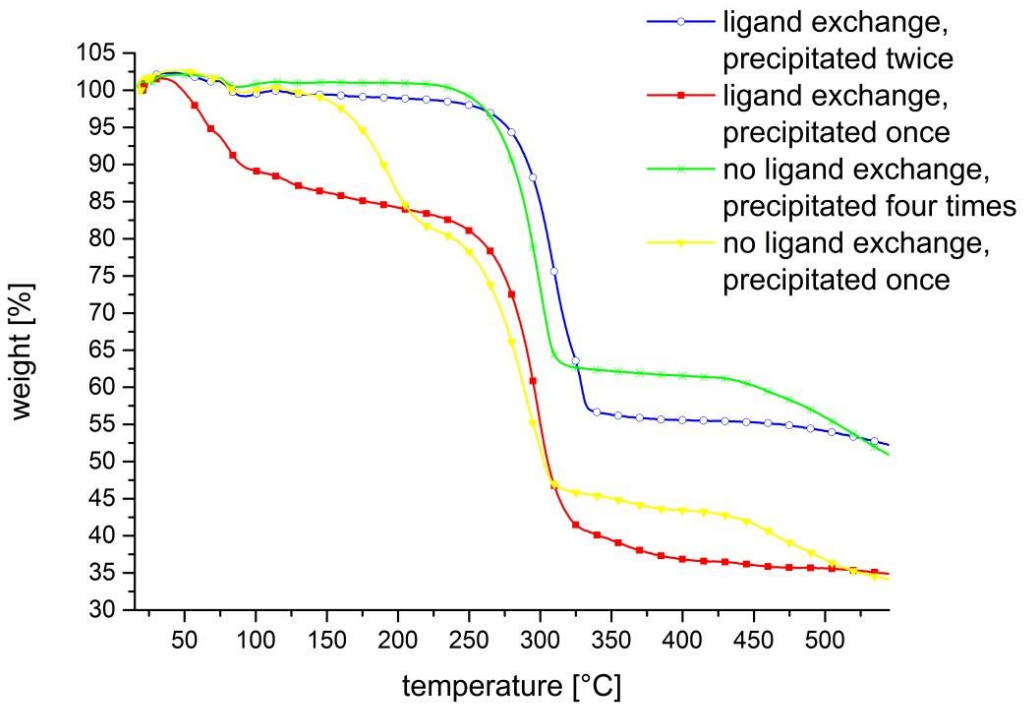

Figure 22: thermo-gravimetric analysis of CIS samples

The nanoparticles themselves do not react at temperatures below 500 °C, therefore, the weight loss is related to the amount of capping agent in the sample. When looking at the graph, it can be seen that the samples that were only precipitated once after the respective reaction (yellow and red line) still contain a considerably larger amount of free ligands. This can be concluded from the higher weight loss between 50 and 250 °C of those two samples, compared to the samples that had been precipitated more often (green and blue line).

Since the samples that were precipitated more often (green and blue line) show no weight loss below 250 °C, it is assumed that those samples did not contain free OA and pyridine, respectively.

Since pyridine is significantly smaller than OA (see figure 23), the weight loss of the sample after ligand exchange was expected to be reduced. However, comparing the blue and the green line the weight loss of the samples before and after ligand exchange appear to be similar. This can be explained with the fact that OA coordinates to the metal surface with a bidentate bond in contrast to pyridine. Thus,

one molecule of OA needs more space and the amount of OA molecules that can coordinate onto the surface of the CIS nanoparticles is smaller.

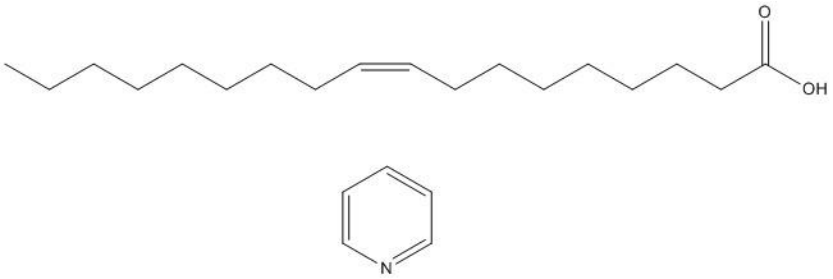

Figure 23: chemical structure of OA (top) and pyridine (bottom)

3.1.2 Hot Injection Method Using Oleic Acid and Hexamethyldisilathiane

The reaction was performed with a variation of the method published by Hines and Scholes[38], using indium(III)oxide and copper(I)oxide, OA and ODE. Hexamethyldisilathiane (HMDS) was injected at 150 °C (see chapter 2.1.2). This method did not yield the desired oleate intermediate products since the oxides were not soluble in OA and ODE. The use of copper(II)oxide instead of copper(I)oxide did not change anything.

Thus, the metal oxides were replaced by indium(III)chloride and copper(II)chloride. With these precursors the reaction yielded CIS nanoparticles, as can be seen in figure 24. However, the resulting nanoparticles were insoluble in toluene.

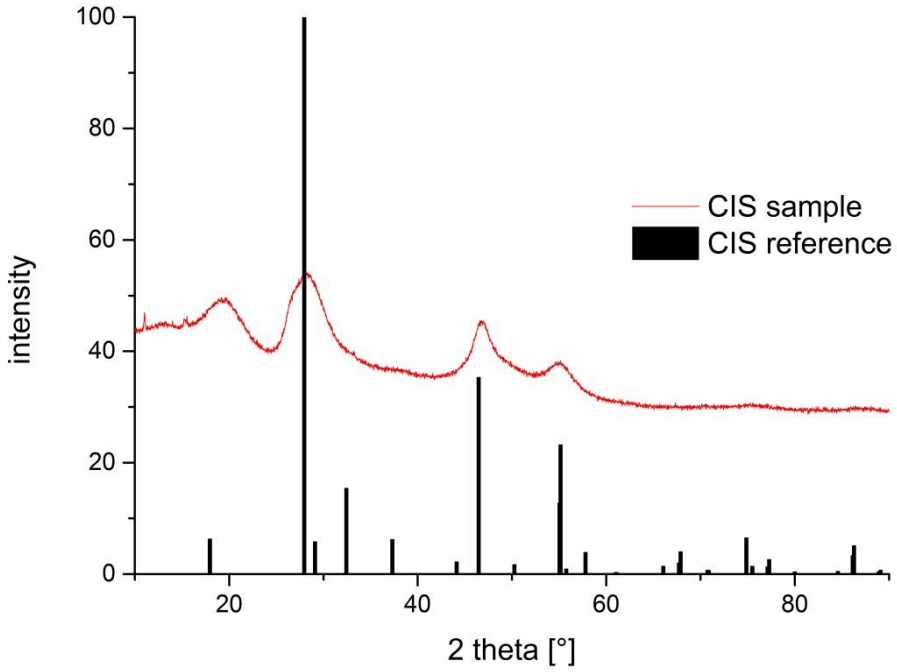

Figure 24: XRD pattern of CIS synthesized with $CuCl_2$ and $InCl_3$

In order to obtain smaller particles and hence increase the solubility, the reaction time after the addition of HMDS was reduced from 5 minutes to 3 minutes. Figure 25 shows, that by reducing the reaction time, the resulting particles became smaller. However, the particles were still insoluble in toluene after precipitation.

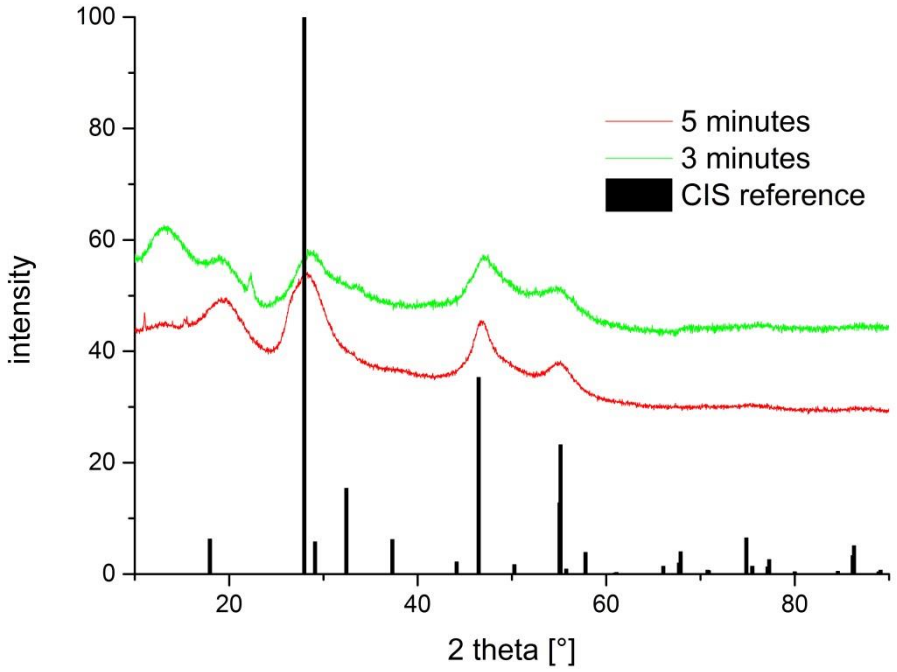

Figure 25: XRD pattern of CIS synthesized with HMDS - different reaction time

The diameter of the particles was estimated using the Scherrer equation (equation 4). The particle size of the nanocrystals that were synthesized with a reaction time of 3 minutes after HMDS injection was around 3.0 nm. The diameter of the particles that were prepared with a reaction time of 5 minutes was approximately 4.4 nm.

The amount of oleic acid was increased stepwise from 1.5 mmol to 4.7 mmol in order to prevent particle agglomeration. When this did not yield the desired solubility of the particles in toluene, the reaction was conducted in 10 ml OA instead of ODE. This was done in order to make sure that there was enough OA in the system to surround the nanoparticles properly. However, the resulting particles were still insoluble.

It was also tried to de-agglomerate the resulting particles. For this purpose they were put into a vial with OA and sonicated for several minutes. However, the product was still insoluble.

Finally, the precursor copper(II)chloride was replaced by copper(I)chloride in order to prevent possible side reactions that come along with the reduction of Cu^{2+} to Cu^{+}.

However, the nanoparticles that were synthesized in this manner were still not soluble.

Since it was not possible to achieve soluble CIS nanoparticles with this synthesis, it was concluded that OA might not be a good capping agent for this preparation. Hence, OA was replaced by 4.5 mmol of OLAM. Other than that, the reaction was performed the same way. The resulting black product after precipitation with acetone was soluble in toluene. However, there was some green precipitate that was not soluble. This indicated that the copper(I)chloride, which is green, had not reacted. Furthermore, it was not possible to precipitate the particles again after they had been dissolved in toluene. Thus, it was concluded, that the reaction with OLAM did not yield a product with the desired properties.

3.1.3 Colloidal Method Using Oleylamine and Dodecanethiol

CIS nanoparticles were synthesized after a method published by Krause C. et al[34], using $In(OAc)_3$, Cu(OAc), trioctylphosphine oxide and oleylamine with a purity of 70%. The copper to indium molar ratio was 1 : 1 (see chapter 2.1.3). The synthesis yielded a black powder that was soluble in chlorobenzene. However the XRD analysis revealed that the product was not CIS. The results of the XRD analysis are shown in figure 26. The four major signals in the sample, at 31°, 36°, 51° and 61° are not present in the references. Therefore, it can be seen that neither of the copper indium disulfide references match the XRD results.

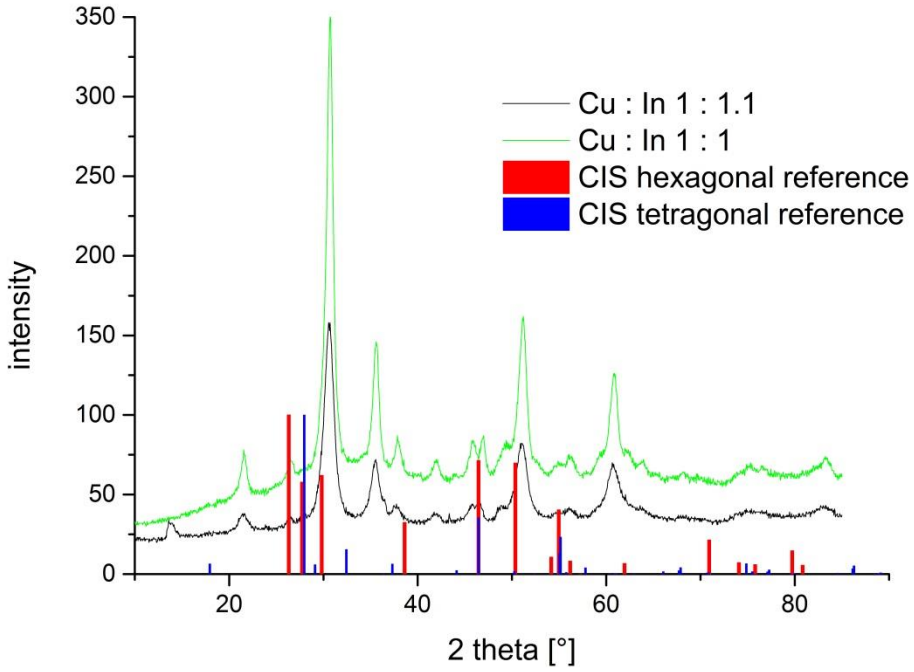

Figure 26: XRD spectra of CIS nanoparticles synthesized with OLAM with different copper to indium molar ratios

Krause et al[34] performed the synthesis with OLAM 80% - 90%. In addition to that the OLAM 70% that was used for the first preparation was old and might have been contaminated. Therefore, the following experiment was done using OLAM 80% - 90% in order to prevent possible side reactions due to contamination.

In reaction systems that contain a high amount of copper-salt the formation of copper-sulfides might be favored. In the interest of preventing the formation of these sulfides, the relative amount of copper was reduced. Furthermore, for solar cells an excess of indium is necessary in order for the material to be n-conducting. Thus, a copper to indium molar ratio of 1 : 1.1 was used. However, the XRD pattern of the CIS nanocrystals, that were prepared that way, showed the same results as the one of the previously synthesized nanoparticles (see figure 26).

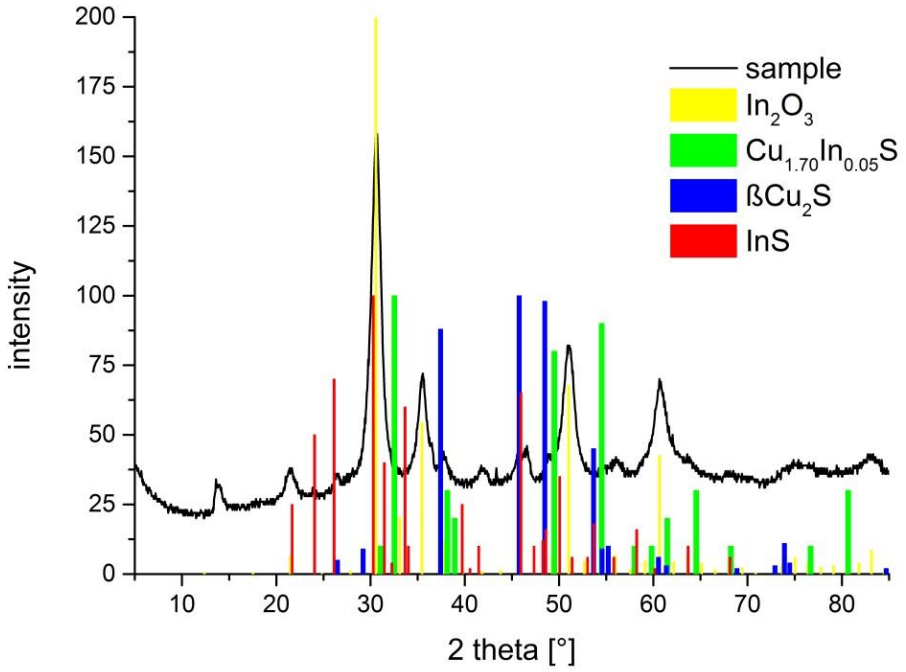

Figure 27: XRD pattern of the synthesized sample with different references

Figure 27 shows the XRD pattern of the sample with various different references. The signal with the highest intensity at 31° (222) correlates with the signals of the indium sulfide and indium oxide references. However, the other three main peaks at 35° (400), 51° (440) and 61° (622) can only be explained with the indium oxide reference. It was assumed, that no oxide could have developed, since the reaction was performed under nitrogen atmosphere. On the other hand, the solvent was not degassed. Therefore, there was probably some oxygen in the reaction system. Thus, it is concluded that the sample consisted mainly of cubic, body-centered indium oxide.

3.1.4 Summary

The CIS synthesis that was performed using copper and indium chlorides and hexamethyldisilathiane did yield the desired product. However, the resulting nanoparticles were insoluble in toluene. While the preparation method using copper and indium acetates, dodecanethiol and oleylamine did not result in CIS nanoparticles. The only synthesis method that yielded soluble CIS nanocrystals was

the preparation that was performed using copper iodide, indium acetate, dodecanethiol and oleic acid (see chapter 3.1.1). Therefore, all further experiments were performed with these nanoparticles.

3.2 Solar Cells

All the solar cell experiments that were performed did not show the expected results. The overall device performances were poor and no improvement could be detected by the introduction of the CIS nanoparticles. The minor differences that have been discovered in the characteristic parameters of the prepared solar cells are discussed in the following chapters.

The organic polymer that was used for the hybrid solar cells was poly[2,7-(9,9-dioctyl-dibenzosilole)-alt-4,7-bis(thiophen-2yl)benzo-2,1,3-thiadiazole] (PSiF-DBT).
PSiF-DBT is a conjugated polymer with a low optical band gap of 1.8 eV.[44] Figure 28 shows the chemical structure of the polymer.

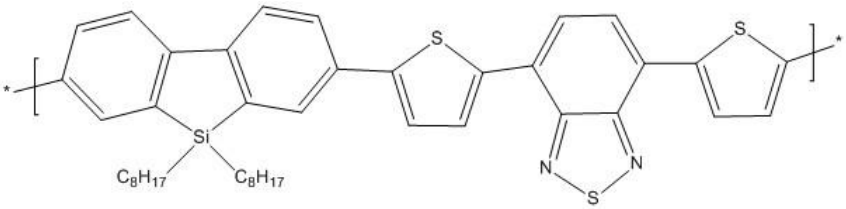

Figure 28: Structure of the conductive polymer PSiF-DBT

3.2.1 No Ligand Exchange

It was tried to build hybrid solar cells with PSiF-DBT as polymer and the CIS nanoparticles that were synthesized with 4.2 mmol 1-DDT and a copper to indium molar ratio of 1 : 1.7. However, it was not possible to generate a uniform film with the prepared polymer nanoparticle solution on top of the PEDOT:PSS layer (see figure 29).

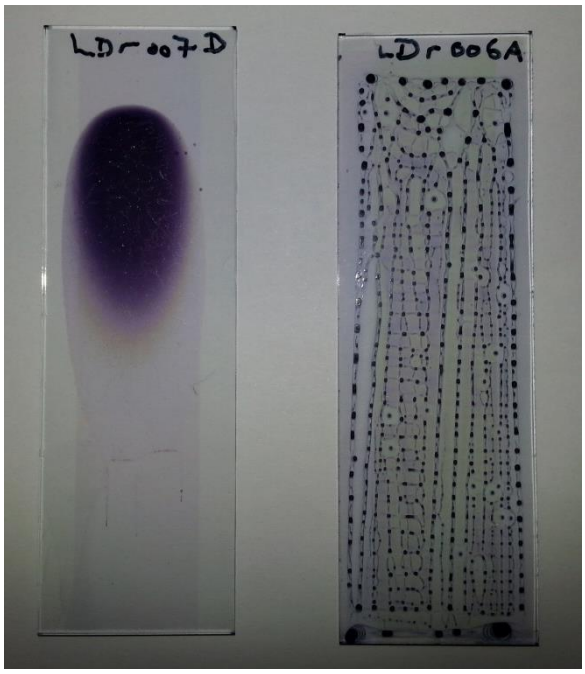

Figure 29: picture of the coating of the active layer on top of the PEDOT:PSS layer

The different appearance of the coatings in the picture is due to the use of different solvents. The active layer was prepared in chlorobenzene (right-hand side of the picture) and in toluene (left-hand side of the picture).

The described coating problems disappeared as soon as the CIS nanoparticles that had been prepared with a lower amount of 1-DDT were used. Thus, it is assumed that the high amount of 1-DDT disturbed the wettability between the two layers.

Solar cells were prepared with a polymer to CIS weight ratio of 1 : 15, containing a polymer concentration of 5 mg/ml. The active layer was doctor-bladed onto the devices with a velocity of 12.5 and 15 mm/s. The resulting devices had an average power conversion efficiency (PCE) of $1.3*10^{-4} \pm 2.9*10^{-5}$%. While the open circuit voltage was relatively high, with values around 0.816 ± 0.114 V, the short circuit current was extremely low ($6.6*10^{-4} \pm 1.3*10^{-4}$ mA/cm²). The measured film thickness of the active layer was between 450 and 650 nm. Thus, it was assumed that the low short circuit current values occurred due to the thick layers. A representative I/V diagram of a solar cell, that has been prepared as described above, is shown in figure 30.

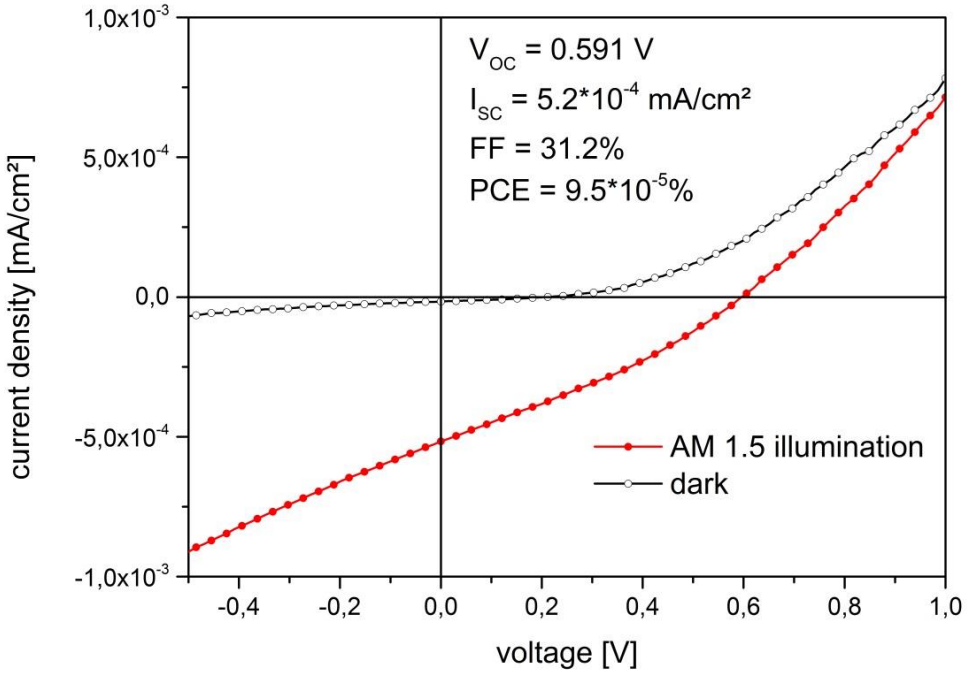

Figure 30: I/V diagram of a typical solar cell with a polymer : CIS weight ratio of 1 : 15, no ligand exchange

The active layer solutions were diluted with chlorobenzene to achieve a lower film thickness. Furthermore, the active layer was doctor-bladed with a velocity of 10 mm/s. Diluting the active layer 1 : 1 led to a film thickness of around 100 nm. This led to a slightly improved I_{SC}, however the V_{OC} decreased. Therefore, the overall performance of the solar cells did not improve.

In order to find out, whether, the performance of the solar cells could be influenced through annealing the devices were tempered at 100 °C for 30 minutes after deposition of the active layer. Thereby the open circuit voltage was reduced by half, which led to a reduced PCE as well.

The weight ratio of polymer : CIS was changed to 1 : 9 so that a lower film thickness could be achieved without such an intensive dilution. Yet, the devices had film thicknesses in a range of 150 to 300 nm. A dilution of 1 : 0.5 yielded layers with a thickness of 100 to 200 nm. However, the devices did not show an improved performance.

A solar cell device, where the active layer consisted only of PSiF-DBT, was built as a reference. These devices had an open circuit voltage of 0.409 ± 0.064 V, a short circuit current of 0.036 ± 0.005 mA/cm² and a PCE of 0.004 ± 6.3*10^{-4}%. Figure 31 shows the I/V curve of one of these solar cells.

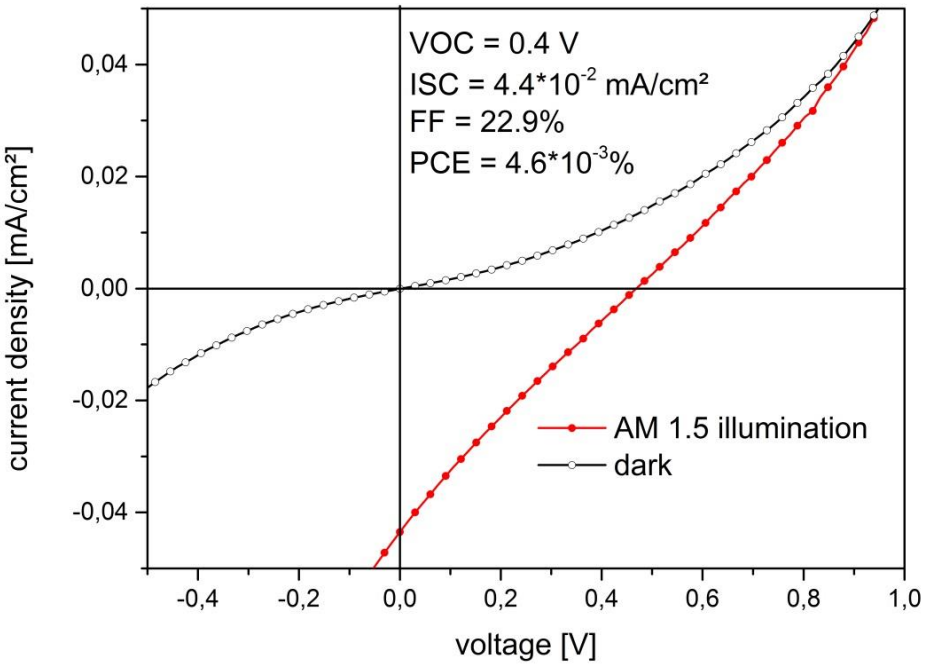

Figure 31: I/V diagram of a solar cell consisting only of PSiF-DBT as an active layer

Hence, the solar cells containing CIS nanoparticles show a worse performance than the devices that are built with an active layer containing only polymer. This might be due to the large ligand shell surrounding the nanoparticles. Another reason could be that the synthesized CIS crystals are not suitable as acceptors in hybrid solar cells.

3.2.1.1 Absorption Measurements of Active Layers

UVVIS measurements were conducted as described in chapter 2.4.3. Figure 32 shows the absorption spectra of active layers containing a varying amount of CIS. From the variation in the absorption of the samples containing CIS (dark blue, light blue and green line) compared to the sample containing only polymer (red line) it is apparent that the absorption of the sample increases with the amount of

nanoparticles present in the sample. The difference in absorption between the different samples decreases at higher wavelengths, indicating that the absorption of the nanoparticles is higher at lower wavelength. However, the absorption of the layers containing nanoparticles is increased over the whole spectrum, indicating that the nanoparticles also absorb at higher wavelengths. Furthermore, the absorption maximum shifts to a slightly higher wavelength for the samples containing nanoparticles.

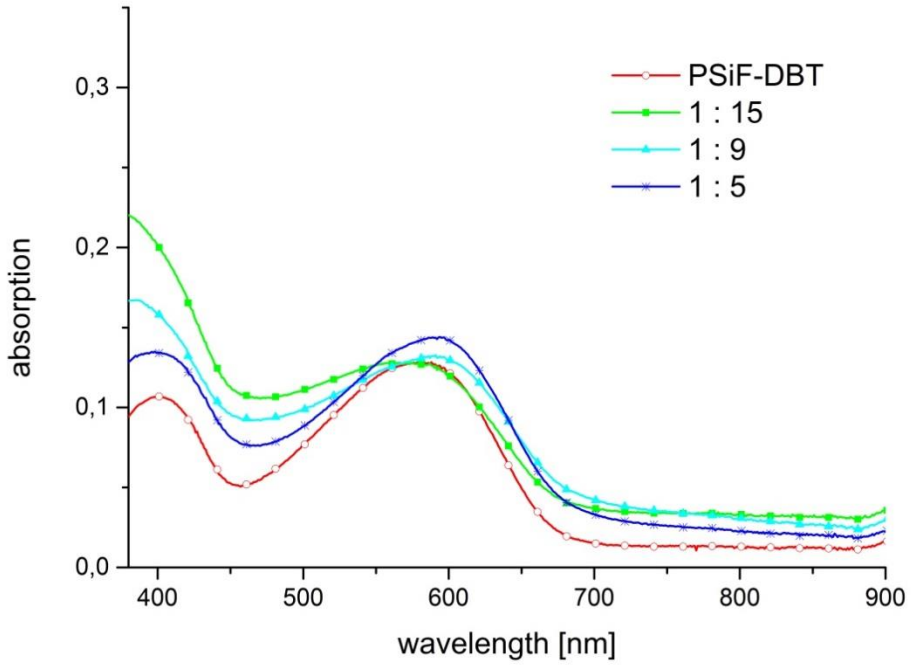

Figure 32: UVVIS of active layers with varying polymer : CIS weight ratios

3.2.1.2 Photoluminescence Quenching Experiments

The charge transfer from the polymer to the nanoparticles essentially influences the performance of a solar cell. When the excited electron is transferred to the nanoparticles, no radiative decay to the ground state can take place. Therefore, if charge transfer occurs, the photoluminescence of the polymer is strongly quenched.[45]

PL (photoluminescence) quenching experiments were conducted as described in chapter 2.4.4. Figure 33 shows the PL spectra of active layers containing a varying amount of CIS nanoparticles. It can be seen in the graph, that the

photoluminescence of the polymer is not reduced by the nanoparticles. Hence it is concluded, that the charge transfer from the polymer to the nanoparticles does not work. This is probably due to the long OA and 1-DDT molecules that surround the nanoparticles and insulate them.

The photoluminescence intensity increases with the amount of nanoparticles present in the active layer. This might be due to the fluorescence of the nanoparticles themselves.

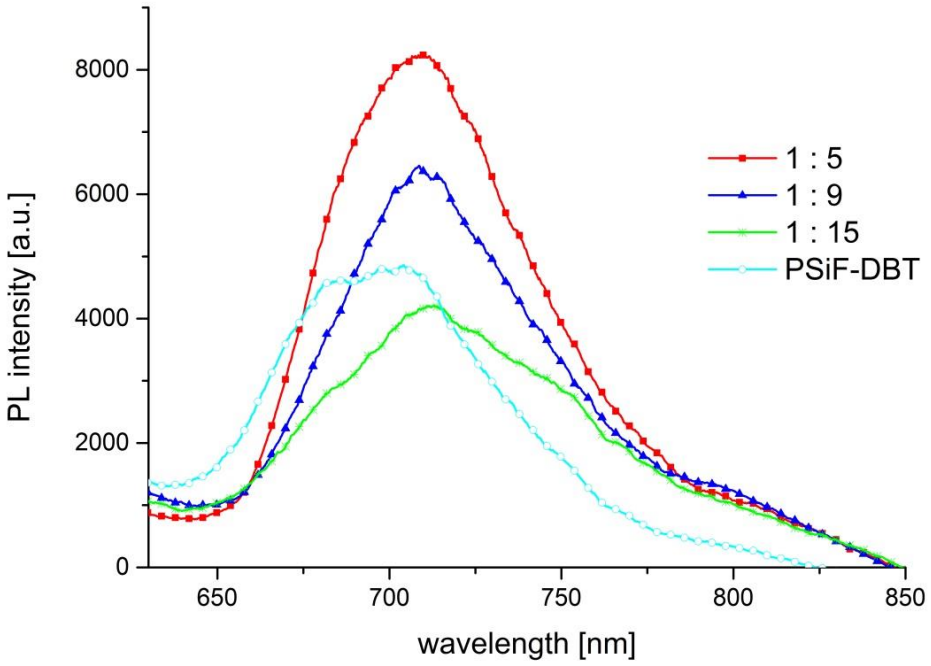

Figure 33: PL spectra of active layers containing a varying amount of CIS

These experiments confirm the necessity of ligand exchange, in order to remove the insulating ligand shell.

3.2.2 Solid State Ligand Exchange with 1,2-Ethanedithiol

Ligand exchange with 1,2-ethanedithiol was performed in solid state after the active layer deposition. Nam M. et al[46] reported a significant improvement of device performance for hybrid solar cells with oleic acid capped PbS nanoparticles as

acceptor material, using this ligand exchange procedure. However, the method does not seem to be applicable for CIS nanoparticles.

3.2.2.1 Bulk Heterojunction assembly

The devices that were built with an additional ligand exchange step with 1,2-ethanedithiol showed a deteriorated performance. The I/V curve of a solar cell that was prepared that way is shown in figure 34. The I/V curve does not have a diode characteristic.

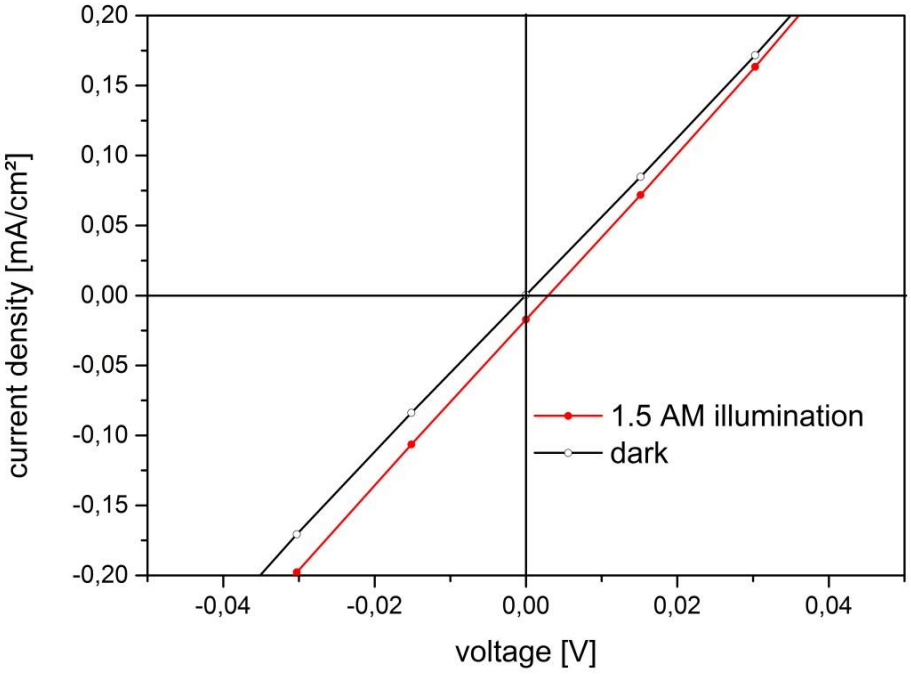

Figure 34: I/V curve of a solar cell treated with 1,2-ethanedithiol

The solid state ligand exchange step was performed outside of the glove box. In order to find out whether the poor performance was due to some reaction of the active layer with oxygen, a device on which no ligand exchange was done was taken out of the glove box for the same amount of time. This solar cell did not show any deterioration when compared to the other devices that were kept inside of the glove box during the whole preparation process. Thus, the working conditions outside of

the glove box were not the reason for the reduced functioning of the devices that had been treated with 1,2-ethanedithiol.

Figure 35 shows a picture of solar cell devices with a polymer active layer, a polymer/CIS active layer and a polymer/CIS active layer that was treated with 1,2-ethanedithiol. The colour of the device where the ligand exchange with 1,2-ethanedithiol had been performed is similar to the colour of the device that had been built without CIS nanoparticles. Since the appearance of the solar cell containing CIS and polymer is very different, it is assumed that at least a part of the nanoparticles was lost during the spin-coating steps of the ligand exchange. This might be due to the small size of the synthesized nanoparticles (see chapter 3.1.1). If that is the case, the morphology of the active layer is destroyed through the spin-coating which would explain the poor performance of the solar cells.

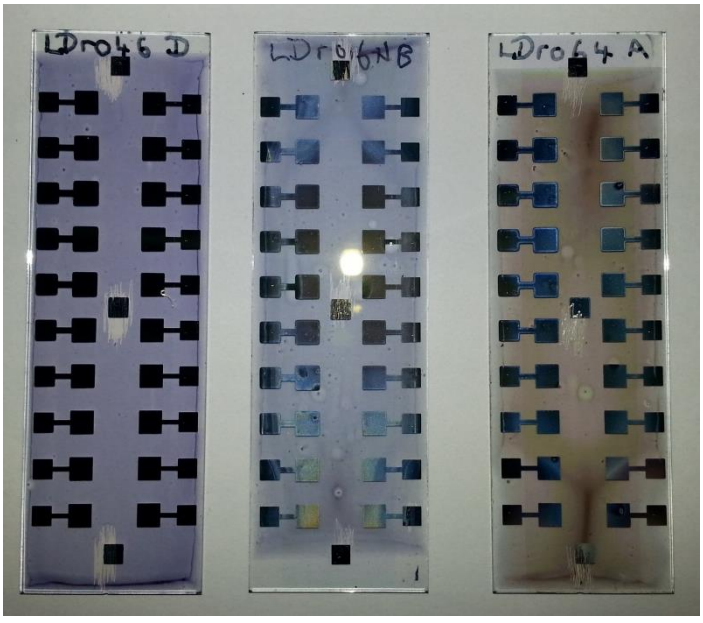

Figure 35: picture of solar cell devices that were made with a polymer active layer (left), a polymer/CIS active layer (right) and a polymer/CIS active layer that was treated with 1,2-ethanedithiol (middle)

3.2.2.2 Inverse Bulk Heterojunction Assembly

Since the ligand exchange with 1,2-ethanedithiol did not lead to an improved device performance, as discussed above, the solar cells were prepared in an inverse bulk

heterojunction assembly. It was hoped that this would lead to better results due to the different device architecture.

The 1,2-ethanedithiol ligand exchange that was performed on the inverse bulk heterojunction solar cells after active layer deposition led to a slight improvement in device performance. The respective I/V curves are shown in figure 36. The fact that the ligand exchange with 1,2-ethanedithiol did work better in the inverse bulk heterojunction assembly, might be due to the different surface under the active layer. It is concluded, that the titanium oxide layer might have helped to prevent the CIS nanoparticles from being washed away during the spin coating step of the ligand exchange.

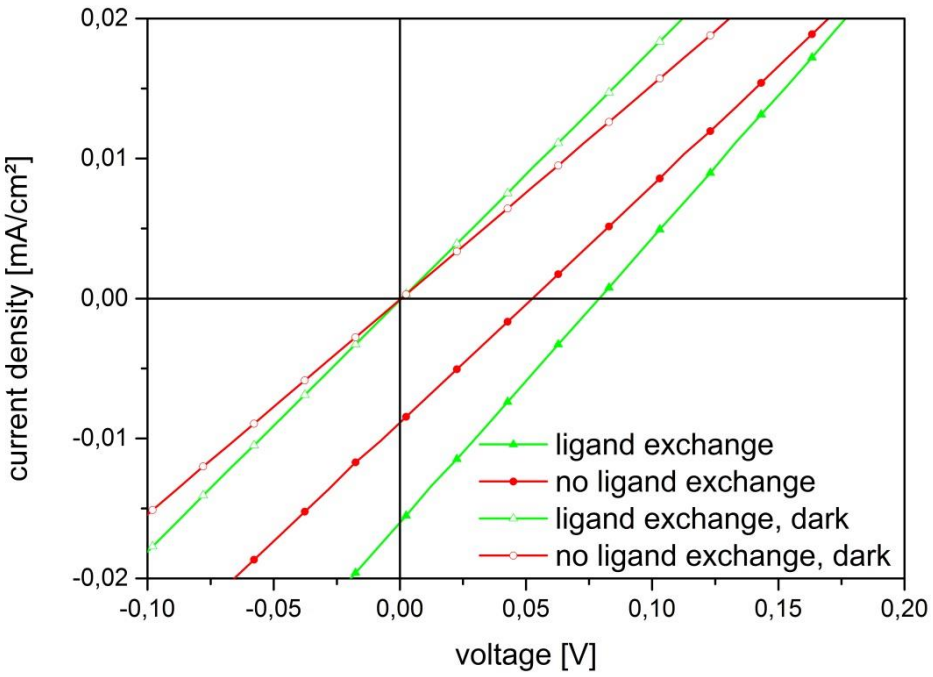

Figure 36: I/V curves of inverse BHJ solar cells built with and without 1,2-ethanedithiol ligand exchange

As can be seen in table 7, the open circuit voltage and the short circuit current are slightly improved by the ligand exchange step. It is noticeable, that especially the short circuit current was higher. Even though the open circuit voltage increased as well, the value was still low. Therefore, the overall performance was only slightly better than that of the BHJ solar cells where no ligand exchange had been performed. Furthermore, the I/V curves do not show any diode characteristics.

Table 7: average characteristic parameters of inverse BHJ solar cells built with and without 1,2 ethanedithiol ligand exchange

	V_{OC} [V]	I_{SC} [mA/cm²]	PCE [%]
no ligand exchange	0.022 ± 0.019	0.004 ± 0.003	$3.3*10^{-5} \pm 3.7*10^{-5}$
ligand exchange, 1,2-ethanedithiol	0.044 ± 0.020	0.116 ± 0.332	$3.9*10^{-4} \pm 7.8*10^{-4}$

3.2.3 Ligand Exchange with Butylamine

Short chained amines are frequently used for ligand exchange on nanoparticles. Radychev N. et al[47] investigated the influence of ligand exchange with different short chained amines on the performance of CdSe / P3HT hybrid solar cells. They reported that the ligand exchange with butylamine led to the best device performances.

Ligand exchange with butylamine was performed in solution before the active layer preparation.

The devices that were built with butylamine capped CIS did not show an improved performance when compared to the solar cells that had been built with CIS where no ligand exchange had been performed. If anything, the introduction of butylamine led to a deterioration of the PCE.

The effect of a temperature treatment on the device performance was investigated. For this purpose, the devices were put on a heating plate for 15 minutes, at a temperature of 140 °C, after the active layer deposition. Figure 37 shows the I/V curves of one solar cell that was subject to an annealing step and of one solar cell that did not receive this treatment. It can be seen that the device that had been tempered shows a better performance. This might be due to free butylamine in the sample, which disturbs the charge transport. It evaporates during the temperature treatment, leading to a better device performance

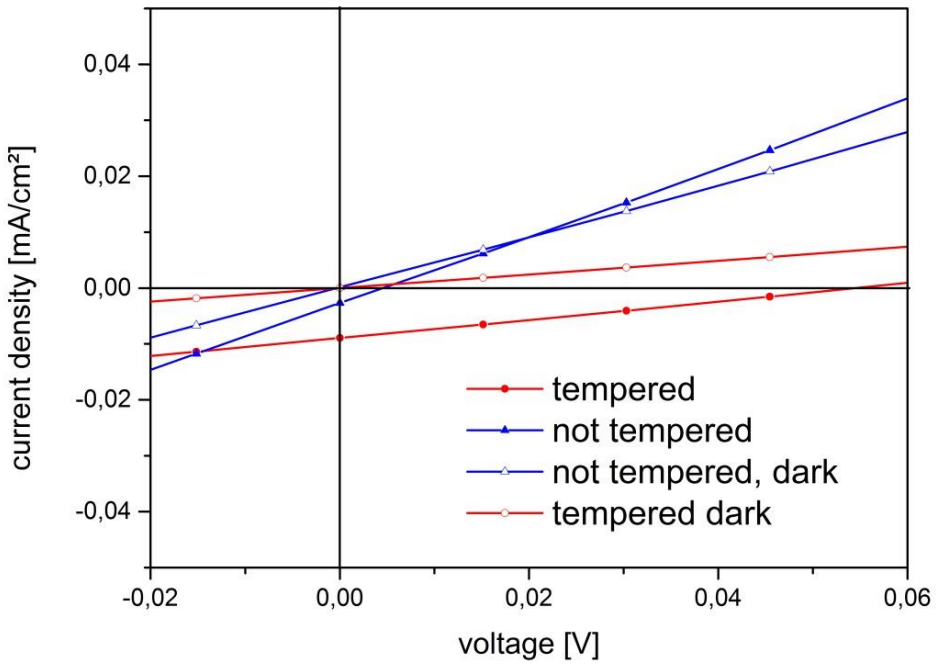

Figure 37: I/V curves of devices that were prepared with butylamine capped CIS, with and without temperature annealing step

Solar cells with different polymer to CIS nanoparticle weight ratios were built. Figure 38 shows the I/V curves of devices that were fabricated with a polymer to CIS weight ratio of 1 : 3, 1: 5, 1 : 9 and 1 : 15. It can be seen, that the solar cells with a smaller amount of CIS are almost short-circuited, while the devices with a higher amount of CIS practically block the current.

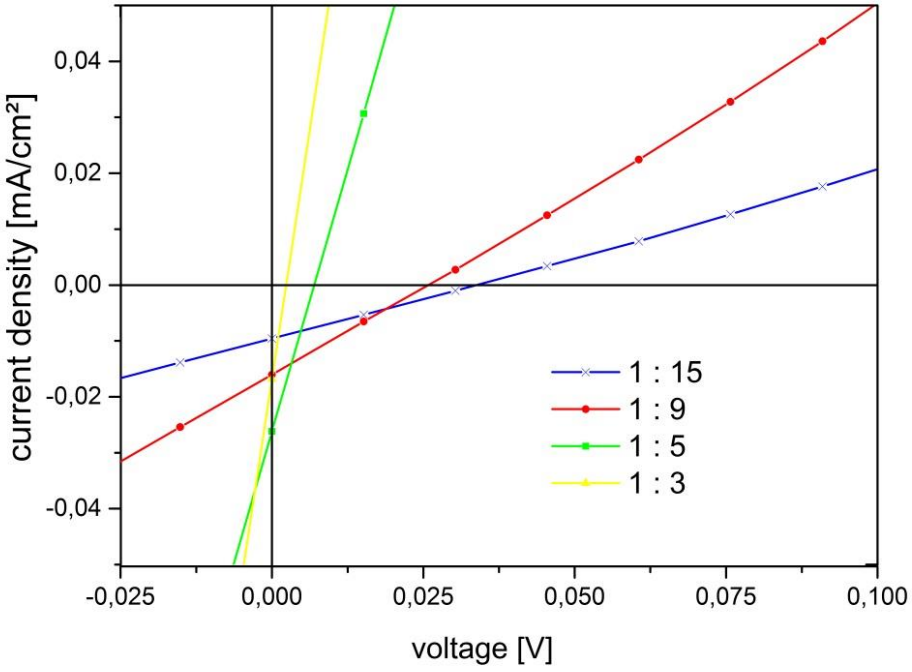

Figure 38: I/V curves of solar cells fabricated with butylamine capped CIS with different polymer to inorganic weight ratios

The performance of solar cells containing butylamine capped nanoparticles can be improved by adding a temperature annealing step and by optimizing the polymer to nanoparticle weight ratio. However, even the devices with the best efficiencies do not show an enhancement in performance when compared to solar cells that had been prepared with CIS nanoparticles on which no ligand exchange had been performed. Furthermore, none of the I/V curves of the devices had a diode characteristic.

Radychev et al. [48] also investigated the influence of ligand exchange with butylamine on the performance of polymer/CIS hybrid solar cells. Since the solar cells did not show an improved PCE after the introduction of butylamine as capper, it was concluded that butylamine might not be a suitable ligand for CIS nanoparticles.

The results of this work are in accordance with the above mentioned literature. Therefore, it is assumed that the ligand exchange butylamine is in fact not applicable as a ligand for CIS nanoparticles. This might be due to OA or 1-DDT coordinating rather strongly to the surface of the nanoparticles and preventing the ligand exchange with butylamine from being successful.

The fact that tempering the devices after active layer deposition improved the performance could also be explained by this theory. If the ligand exchange did not work, there is only free butylamine in the CIS sample. During the temperature annealing step the free butylamine evaporates, thus, leading to a better performance of the resulting solar cells.

3.2.4 Ligand Exchange with Pyridine

Pyridine is a small and volatile molecule with a weak binding ability. It is widely used as a small ligand that provides surface passivation and allows for good solution processing. Pyridine capped nanoparticles can be brought in very close contact with the polymer in the active layer. Thus the contact resistance and recombination loss decreases and the charge transport is enhanced.[49]

3.2.4.1 Bulk Heterojunction Assembly

The active layers that were prepared with polymer and pyridine capped CIS nanoparticles with chlorobenzene as a solvent, showed similar wetting problems as described at the beginning of chapter 3.2. In order to avoid this behavior, chloroform was used as a solvent. The films that were deposited with chloroform were significantly more uniform. The layers could be further improved by reducing the temperature during the doctor blading process to room temperature. Figure 39 shows the picture of devices, where the active layer was applied using chlorobenzene (left), chloroform (middle) and chloroform at a room temperature (right).

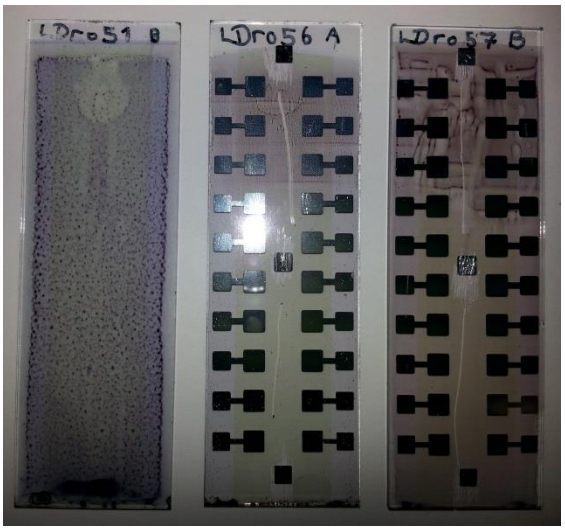

Figure 39: picture of active layers that were applied using chlorobenzene, chloroform and chloroform at room temperature

Since the layer deposition worked best at room temperature with chloroform as a solvent, all the following devices that were built with pyridine capped CIS nanocrystals were prepared under these conditions.

The devices built with pyridine capped CIS did show an improved performance compared to solar cells that had been built without ligand exchange. The I/V curves of solar cells built with pyridine capped CIS and with CIS nanoparticles had not been subject to ligand exchange, are compared in figure 40. It can be seen that I_{SC} increases significantly, while the V_{OC} values do not change. This was to be expected since the nanoparticles are now surrounded by a smaller ligand shell. Thus the charge transport is facilitated.

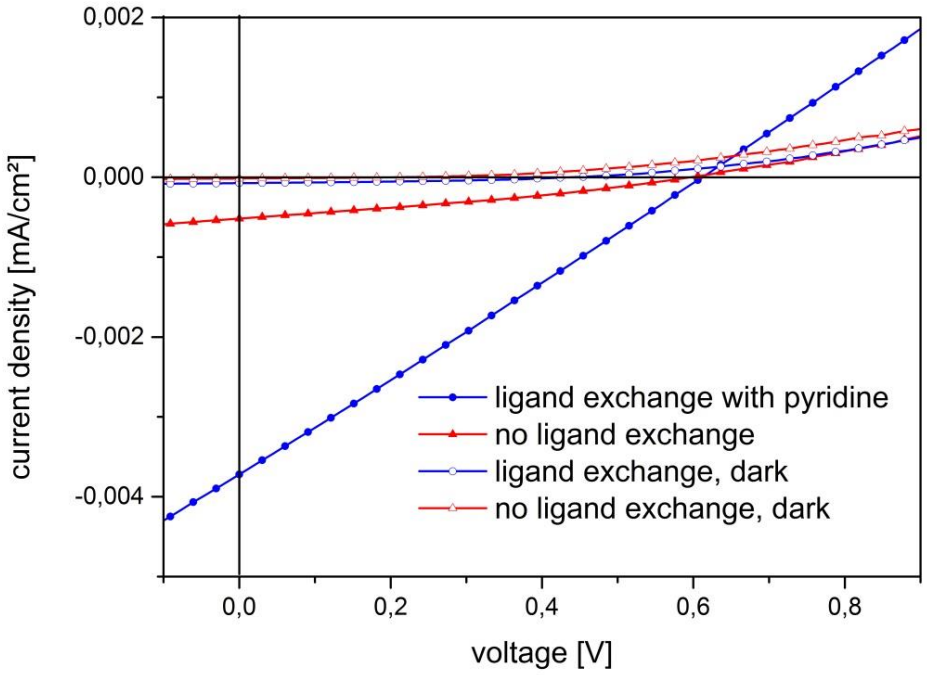

Figure 40: I/V curves of a solar cell built with CIS nanoparticles capped with pyridine and OA

However, the device that was built with an active layer that contained only polymer still showed a significantly higher performance (see figure 41). Especially the I_{SC} of the device with the pure polymer layer was considerably higher.

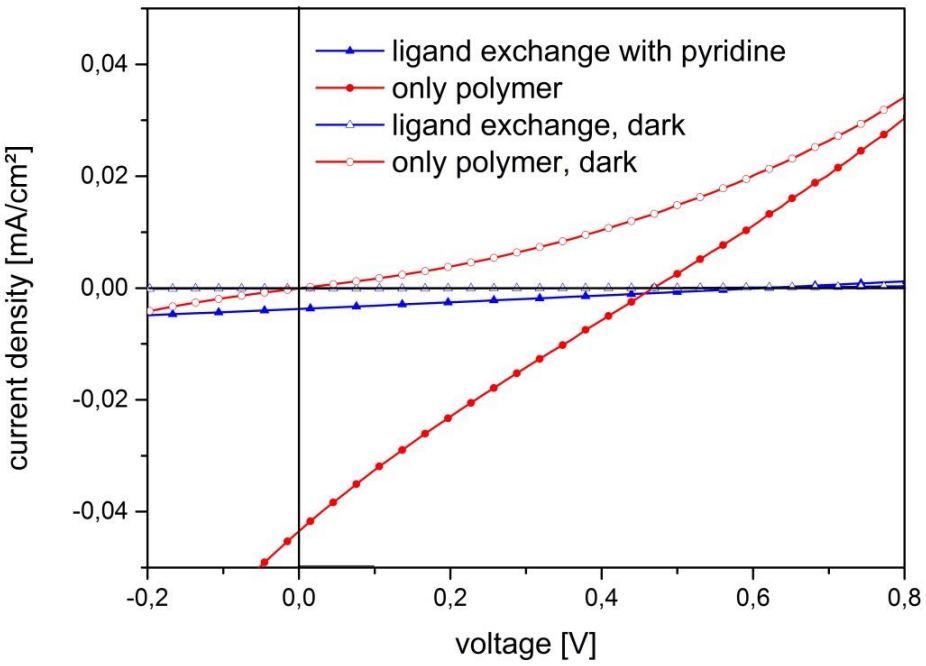

Figure 41: I/V curves of a solar cell built with pyridine capped CIS and without CIS

Experiments were done in order to get information about which polymer to nanoparticles weight ratio would yield the best cell performance. For this purpose, active layers with three different PSiF-DBT to CIS weight ratios were prepared. The I/V curves of the resulting solar cells are shown in figure 42. It can be seen, that the devices which were built with a lower amount of CIS had a better performance. While the V_{OC} values are very similar to each other, the I_{SC} increases with a decreasing amount of CIS in the layer. Therefore, it is assumed that the disturbance of the charge transport by the ligand shell of the nanoparticles is higher than the improvement of the performance through the nanoparticles themselves.

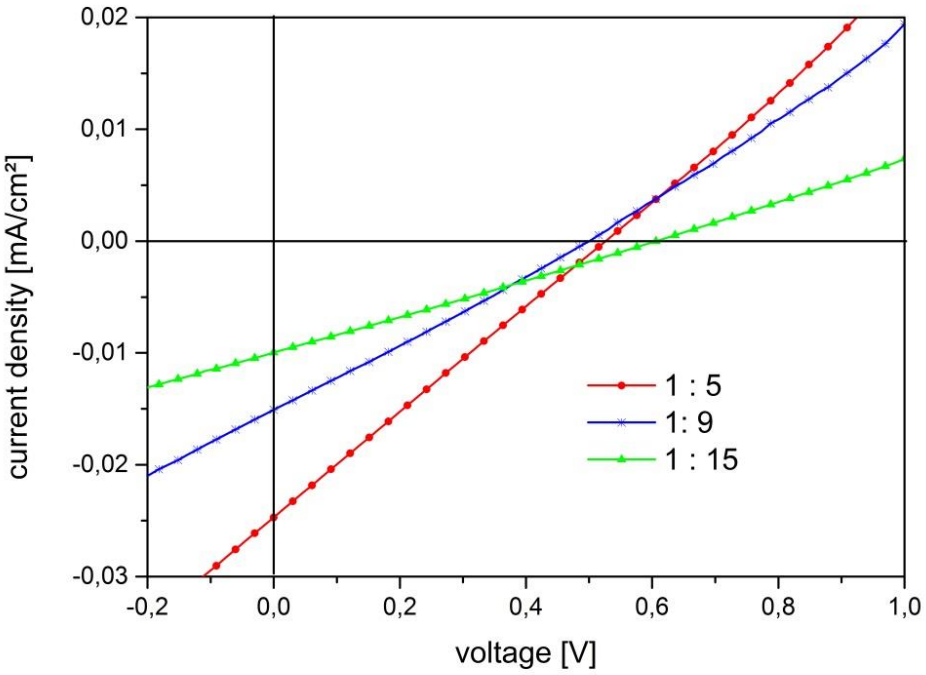

Figure 42: I/V curves of solar cells built with different polymer to CIS weight ratio

The influence of a temperature annealing step on the solar cell performance was also investigated. For this purpose, the device was put on a heating plate at 140 °C for 15 minutes after the active layer deposition. From the I/V curves shown in figure 43 it can be concluded that the solar cell PCE deteriorated significantly if the device was exposed to temperature treatment.

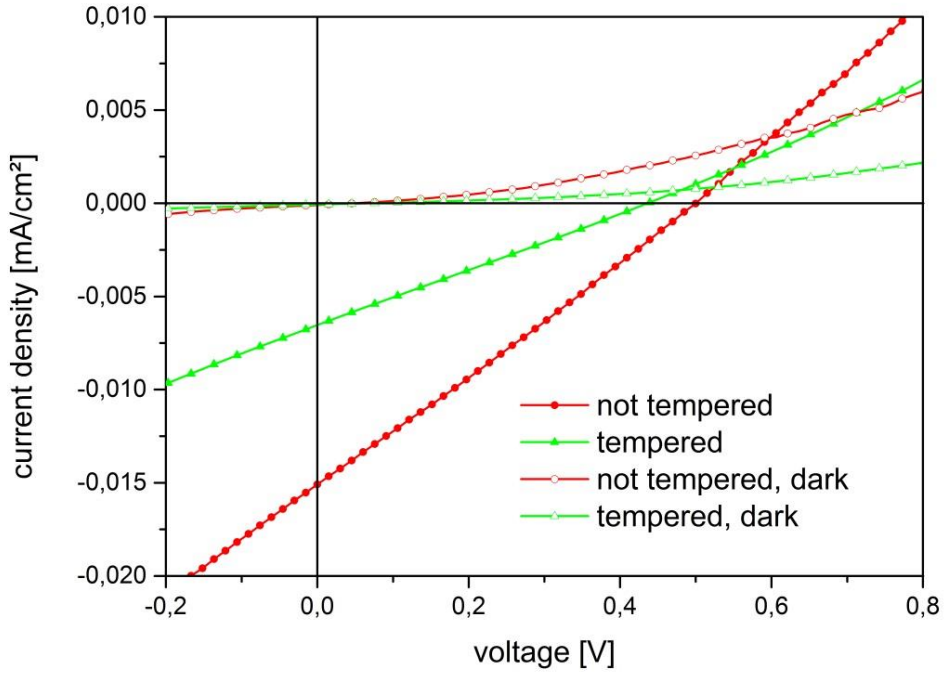

Figure 43: I/V curves of a tempered and non-tempered solar cell

3.2.4.1.1 Investigation of different Copper to Indium Ratios

The band gap of CIS nanoparticles can not only be influenced by the size of the crystals but also by the composition. In particles with a lower amount of Cu, the valence band is lowered. Thus, the band gap is enlarged in these particles.[28]

CIS nanoparticles were synthesized using two different copper to indium molar ratios, namely 1 : 1 and 1 : 1.7. Solar cells were built using both pyridine capped CIS products. I/V curves of both types solar cells are shown in figure 44. The I_{SC} is slightly higher in the device where a copper to indium ratio of 1 : 1 was used. On the other hand, the V_{OC} of the solar cell that was built using a copper to indium ratio of 1 : 1.7 is marginally higher. All in all, no significant difference could be detected between the two different copper to indium ratios.

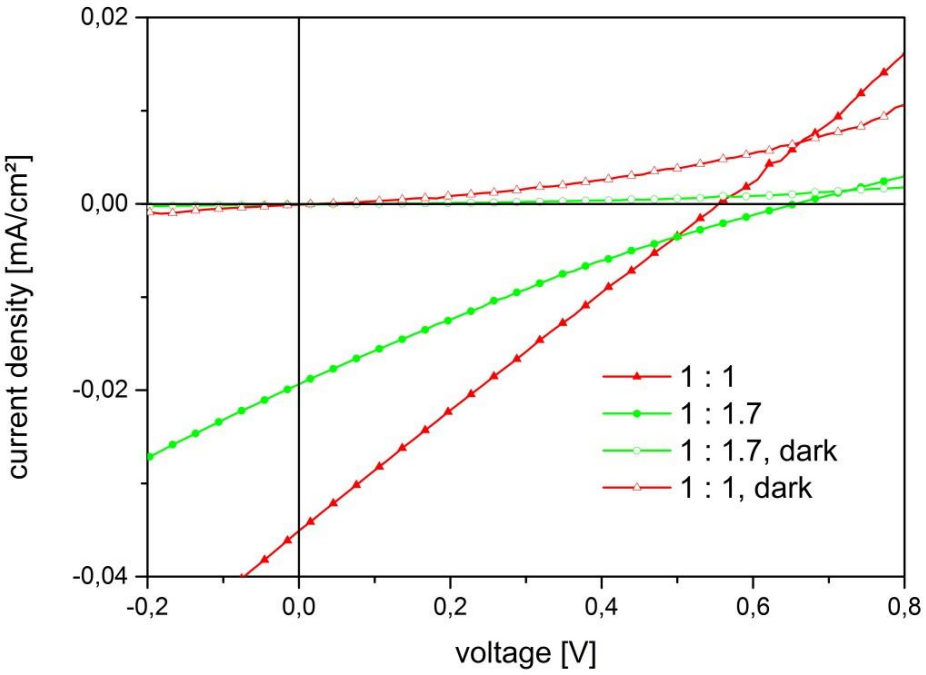

Figure 44: I/V curves of solar cells built with different copper to indium molar ratios

3.2.4.1.2 UVVIS Measurements of Active Layers

UVVIS measurements of the active layers were conducted as described in chapter 2.4.3. The resulting absorption spectra are shown in figure 45. The absorption rises with the amount of CIS nanoparticles in the layer. The difference in the absorption increases at lower wavelengths. Thus, it is concluded that the absorption of the nanoparticles is higher at these wavelengths. However, there is still a difference in absorption at higher wavelengths, therefore, it is deduced that the nanoparticles absorb light up to a wavelength of 900 nm.

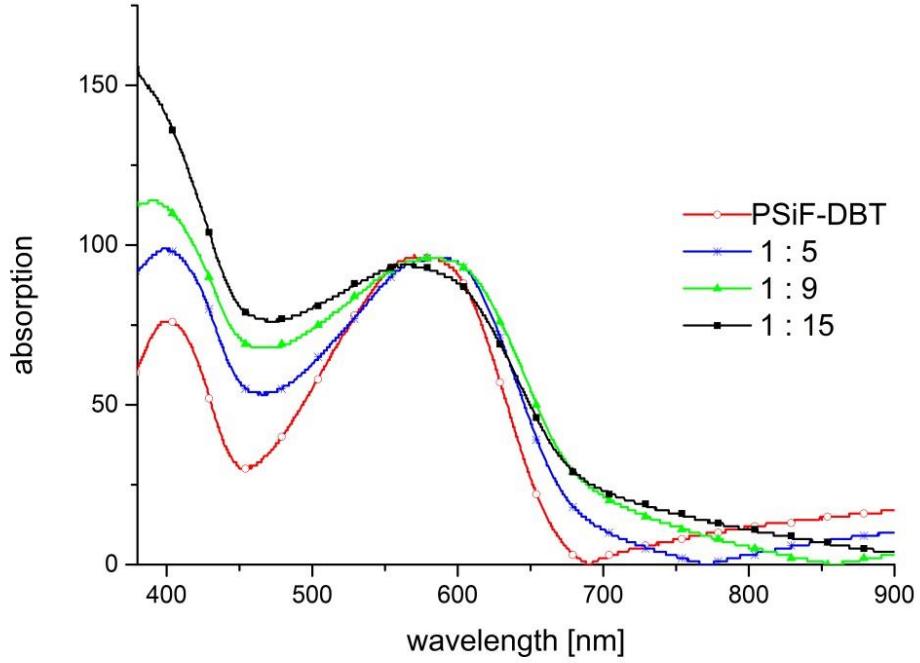

Figure 45: UVVIS of active layers built with pyridine capped CIS with a varying amount of nanoparticles

3.2.4.1.3 PL Quenching Experiments of Active Layers

Photoluminescence quenching experiments were performed as described in chapter 2.4.4. The quenching was expected to work better than with the OA capped nanoparticles, since the pyridine molecules are significantly smaller. However, as can be seen in figure 46, no trend in the reduction of photoluminescence intensity can be observed. Hence, the electron transfer between the polymer and the nanoparticles does not work even after ligand exchange with pyridine. This could explain the still very poor performance of the solar cells that had been prepared with pyridine capped CIS.

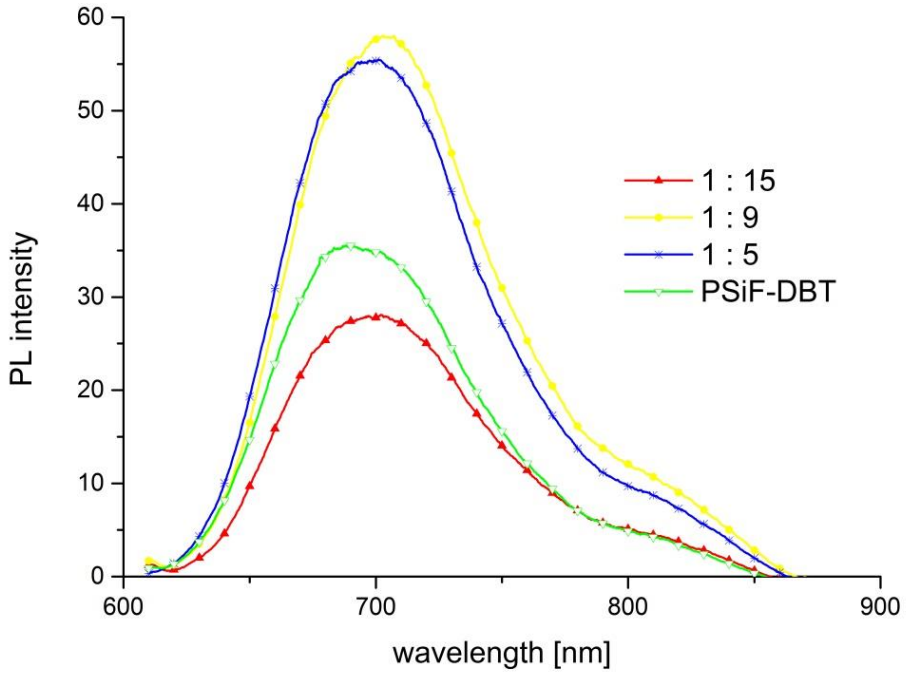

Figure 46: photoluminescence spectra of active layers containing a varying amount of pyridine capped CIS nanoparticles

3.2.4.2 Inverse Bulk Heterojunction Assembly

In order to investigate the influence of the device architecture on the solar cell performance, inverse bulk heterojunction devices were prepared.

The solar cells that were built with an inverse bulk heterojunction assembly showed an improvement in performance when compared to the bulk heterojunction assembly devices (see figure 47). The V_{OC} of inverse BHJ devices was lower than that of BHJ devices. However, the I_{SC} was significantly higher. Altogether, this results in an increased performance.

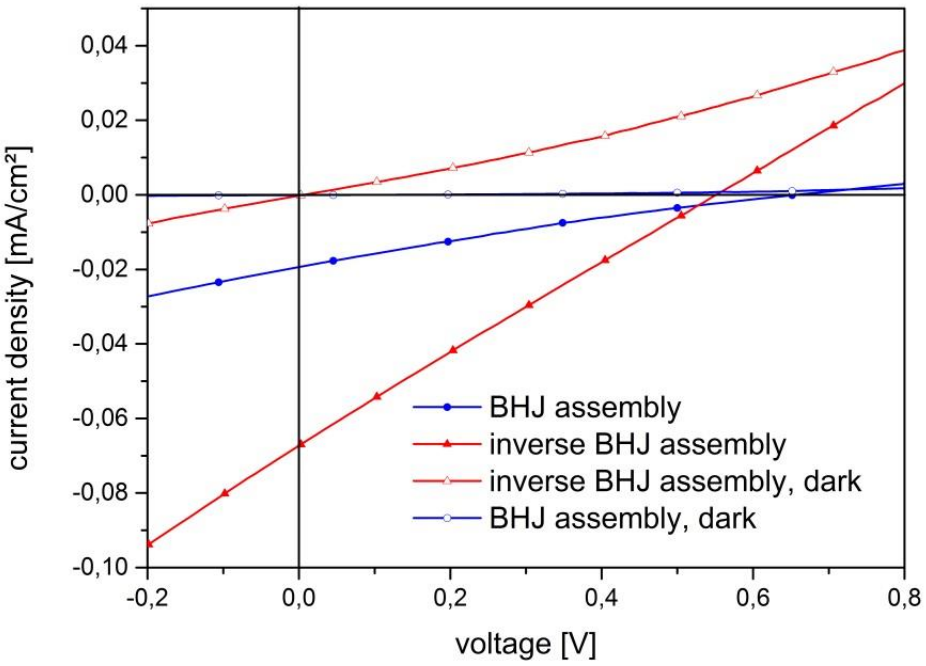

Figure 47: comparison of I/V curves of a BHJ assembly and an inverse BHJ assembly solar cell

However, the performance of the solar cells that were built with an active layer consisting only of polymer was still higher, as can be seen in figure 48.

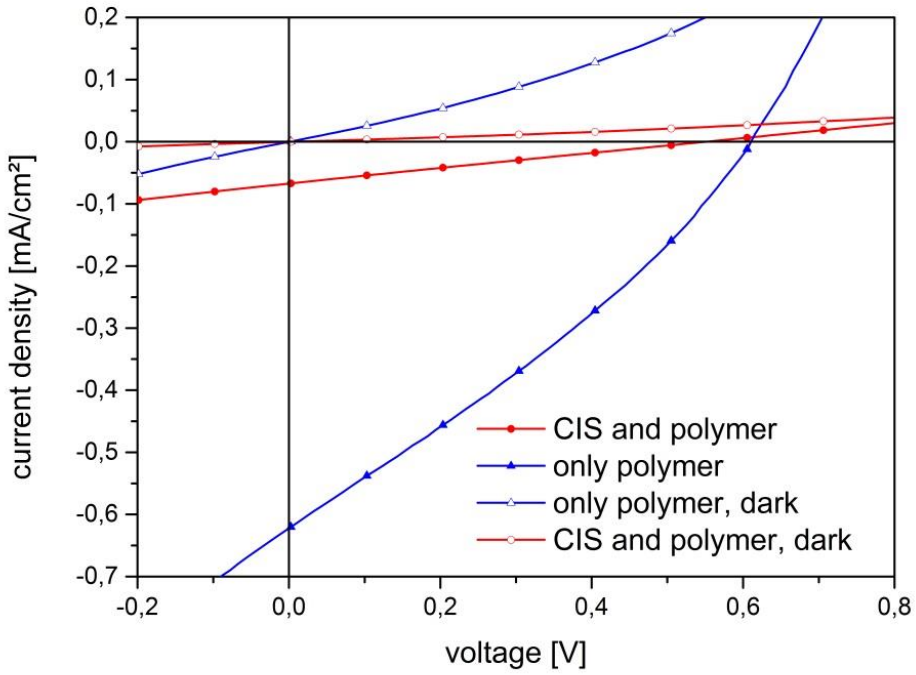

Figure 48: I/V curves of a pyridine capped CIS/polymer and a polymer inverse BHJ solar cell

In table 8 the average characteristic parameters of a bulk heterojunction, an inverse bulk heterojunction and a polymer solar cell are compared.

Table 8: average characteristic parameters of a BHJ, an inverse BHJ and a polymer solar cell built with pyridine capped CIS

	V_{OC} [V]	I_{SC} [mA/cm²]	PCE [%]
BHJ	0.535 ± 0.214	0.016 ± 0.003	$1.9*10^{-3} \pm 7.8*10^{-4}$
inverse BHJ	0.444 ± 0.093	0.049 ± 0.017	$5.6*10^{-3} \pm 2.5*10^{-3}$
polymer, inverse	0.310 ± 0.239	0.384 ± 0.476	$4.4*10^{-2} \pm 4.7*10^{-2}$

3.2.4.2.1 Solid State Pyridine Ligand Exchange

Lefrançois A. et al[50] investigated the effects of post-deposition solid state ligand exchange with different short chained molecules. Amongst others, pyridine was examined for this procedure.

A pyridine ligand exchange was performed in solid state, after the deposition of the active layer (see chapter 2.3.1). This did lead to an improvement of the performance (see figure 49). However, the performance of both devices was not good (see table 9).

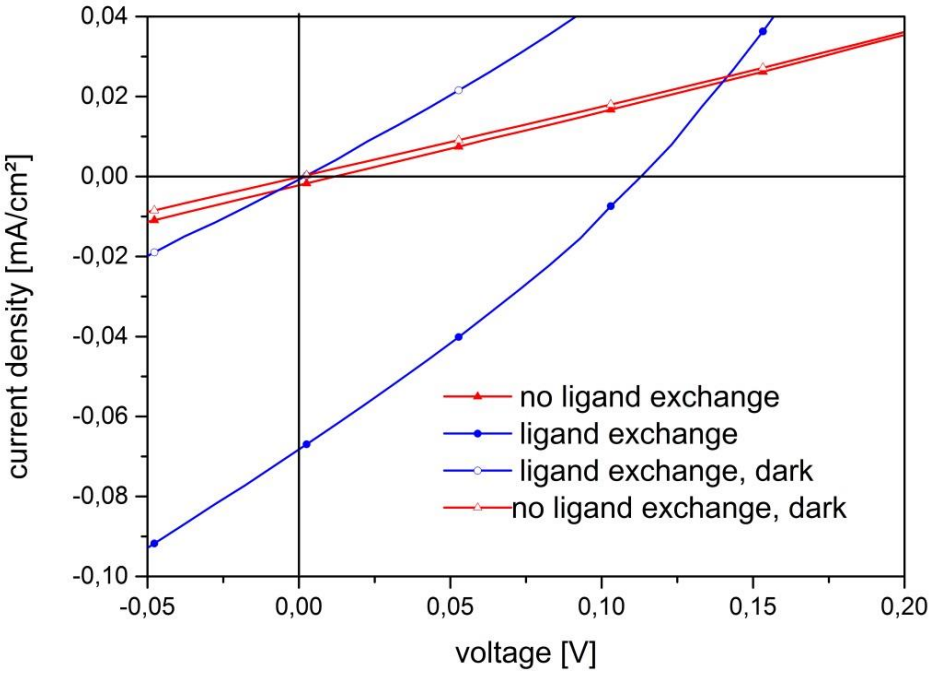

Figure 49: I/V curves of solar cells with and without pyridine solid state ligand exchange

In table 9 the average characteristic parameters of a bulk heterojunction and an inverse bulk heterojunction solar cell are compared. It is noticeable, that the open circuit voltage decreases drastically in the inverse bulk heterojunction assembly. On the other hand, the inverse bulk heterojunction devices show a significantly higher short circuit current. The overall PCE of both types of solar cells is similarly low.

Table 9: comparison of average characteristic parameters of a bulk heterojunction and inverse bulk heterojunction solar cell with no ligand exchange as well as an inverse bulk heterojunction solar cell with pyridine solid state ligand exchange

	V_{OC} [V]	I_{SC} [mA/cm²]	PCE [%]
BHJ, no ligand exchange	0.471 ± 0.195	0.002 ± $4.6*10^{-4}$	$2.3*10^{-4}$ ± $9.5*10^{-5}$
inverse BHJ, no ligand exchange	0.005 ± 0.004	0.057 ± 0.251	$1.4*10^{-4}$ ± $6.2*10^{-4}$
inverse BHJ, pyridine solid state ligand exchange	0.031 ± 0.038	0.054 ± 0.022	$7.3*10^{-4}$ ± $8.4*10^{-4}$

The solid state pyridine ligand exchange leads to a slight increase of V_{OC}. This leads to a small increase in PCE. However, the performance of both devices was rather low. Therefore, no consequential conclusion can be drawn. Thus, it is assumed that the time of the treatment with pyridine was too short in order for the ligand exchange to be successful.

4 Summary and Outlook

The aim of this thesis was to synthesize CIS nanoparticles with a varying copper to indium molar ratio and perform ligand exchange on the prepared nanoparticles. Subsequently, the nanoparticles were to be introduced into hybrid solar cells and the effects of the ligand shell as well as the stoichiometry (copper to indium molar ratio) on device performance were to be investigated.

The CIS synthesis that was performed using CuI and $In(OAc)_3$ as precursors, 1-dodecanethiol as a sulfur source and capping agent and oleic acid as a ligand turned out to be not as easy as expected. The molar ratio of total copper and indium salt to 1-dodecanethiol had a major impact on the product. Thus, the synthesis method yielded a gel if the molar ratio was too low and side products if the molar ratio was too high. However, it was possible to prepare CIS nanoparticles with different copper to indium molar ratios after the optimum molar ratio had been found.

The preparation method using HDMS as a sulfur source, oleic acid as a capping agent and copper and indium chlorides as precursors did yield CIS nanoparticles. However, it was not possible to prevent the agglomeration of the resulting product. Thus, the synthesized nanoparticles were insoluble and, therefore, not applicable for hybrid solar cells. The aggregation might be due to oleic acid not being an appropriate capping agent for CIS nanocrystals that are prepared with this method.

The synthesis, where copper and indium acetate were used as the respective precursors, a mixture of 1-dodecanethiol and t-dodecanethiol as sulfur source and oleylamine as capping agent, did not yield CIS as a product. The copper to indium molar ratio was changed in order to reduce the amount of copper in the reaction mixture and, thus, prevent the formation of copper sulfides. However, the resulting product showed the same x-ray diffraction pattern, indicating that the product had not changed.

Solar cells were prepared using the CIS nanoparticles that were synthesized with CuI, $In(OAc)_3$, 1-dodecanethiol and oleic acid as acceptor material. The conductive polymer PSiF-DBT was introduced as donor material. The resulting devices showed a very poor performance. This was mainly due to the low short circuit current and fill factor. Since the active layer had a very high film thickness, the active layer solution

was diluted in order to achieve thinner layers and thereby higher short circuit current values. However, this did not have any influence on the device performance.

Photoluminescence quenching experiments were conducted on the active layers containing a varying amount of CIS nanoparticles. There was no observable trend of a reduced photoluminescence intensity correlating to the amount of CIS present in the active layer. Therefore, it is concluded that the charge transfer from the polymer to the nanoparticles does not work. This is probably due to the ligand shell surrounding the CIS nanocrystals.

The introduction of CIS that had been subject to a ligand exchange with pyridine, into solar cells yielded a significant improvement of the performance. However, the reference device that had been built containing only polymer in the active layer was still slightly better. The photoluminescence quenching experiments that were performed on these active layers showed that the charge transfer from the polymer to the nanoparticles still did not work properly. Thus, it is concluded that the ligand exchange step had only worked partially and there were still oleic acid or 1-dodecanethiol molecules on the surface of the nanoparticles, inhibiting the charge transfer.

Solar cells built with pyridine capped CIS, using an inverse bulk heterojunction assembly, had a better performance than the ones built using a bulk heterojunction assembly. However, both reference devices that were built with an active layer consisting only of polymer had an even better performance.

The solid state ligand exchange performed with pyridine did yield an improvement in device PCE. However, compared to the solar cells that had been built with CIS where the pyridine ligand exchange had been performed before device fabrication, the performance was inferior.

Solar cells that were built with butylamine capped CIS nanoparticles showed a very poor performance. This might be due to butylamine not being an appropriate capping agent for CIS nanocrystals. Another reason could be that the ligand exchange had not worked and the resulting product contained free butylamine in addition to the oleic acid capped nanoparticles. This would explain the increase in performance after tempering the devices, since the free butylamine would evaporate during this step.

The addition of a solid state ligand exchange step with 1,2-ethanedithiol after the active layer deposition did not yield successfully functioning solar cells. It is suspected, that the nanoparticles are washed out of the layer during the spin coating step due to their small particle size. Thus, the morphology of the active layer is destroyed, leading to a deterioration of the device performance.

The solid state ligand exchange with 1,2-ethanedithiol in solar cells that were built using an inverse bulk heterojunction assembly did lead to an improvement in device performance. Hence, it is concluded that the ligand exchange with 1,2-ethanedithiol did work at least partially. The different surface underneath the active layer in the inverse bulk heterojunction assembly might prevent the CIS nanoparticles from being washed away during the spin coating step.

The average characteristic parameters of the solar cells built with CIS capped with different ligands are summarized in table 10.

Table 10: summary of the characteristic parameters of the solar cells

	ligand exchange	V_{OC} [V]	I_{SC} [mA/cm²]	P_{CE} [%]
BHJ	no ligand exchange	0.471 ± 0.195	$0.002 \pm 4.6*10^{-4}$	$2.3*10^{-4} \pm 9.5*10^{-5}$
	butylamine	0.040 ± 0.014	0.014 ± 0.003	$1.3*10^{-4} \pm 2.8*10^{-5}$
	pyridine	0.535 ± 0.214	0.016 ± 0.003	$1.9*10^{-3} \pm 7.8*10^{-4}$
	1,2-ethanedithiol	0.356 ± 0.149	$7.5*10^{-4} \pm 2.5*10^{-4}$	$6.6*10^{-5} \pm 3.8*10^{-5}$
	only polymer	0.409 ± 0.064	0.036 ± 0.005	$3.5*10^{-3} \pm 6.3*10^{-4}$
inverse BHJ	no ligand exchange	0.022 ± 0.019	0.004 ± 0.003	$3.3*10^{-5} \pm 3.7*10^{-5}$
	pyridine	0.444 ± 0.093	0.049 ± 0.017	$5.6*10^{-3} \pm 2.5*10^{-3}$
	solid state pyridine	0.031 ± 0.038	0.054 ± 0.022	$7.3*10^{-4} \pm 8.4*10^{-4}$
	1,2-ethanedithiol	0.044 ± 0.020	0.116 ± 0.332	$3.9*10^{-4} \pm 7.8*10^{-4}$
	only polymer	0.310 ± 0.239	0.384 ± 0.476	$4.4*10^{-2} \pm 4.7*10^{-2}$

Further research should be directed towards better understanding the ligand exchange step and finding suitable ligands for CIS nanoparticles. However, there has already been a lot of research directed on CIS nanoparticles and their application in solar cells. Until now, for solar cells built with CIS synthesized via a colloidal method, there are no reports of efficiencies exceeding 1%. Rath et al.[2] reported efficiencies of 2.8%. However, the nanoparticles had been prepared via the in situ route. Therefore, it might be reasonable to research other non-toxic inorganic nanoparticle materials for hybrid solar cells.

5 Abbreviations

- CB … Chlorobenzene
- CIS … Copper indium disulfide
- DDT … Dodecanethiol
- HMDS… Hexamethyldisilathiane
- HOMO … Highest occupied molecular orbital
- IR … Infrared
- ITO … Indium tin oxide
- LUMO … Lowest unoccupied molecular orbital
- MEH-PPV … Poly[2-methoxy-5-(2-ethyl-hexyloxy)-1,4-phenylene vinylene]
- OA … Oleic acid
- ODE … 1-octadecene
- OLAM … Oleylamine
- P3HT … Poly(3hexylthiophene-2,5-diyl)
- PCPDTBT … Poly[2,6-(4,4-bis-(2-ethyl-hexyl)-4H-cyclopenta[2,1-b;3,4-b]- dithiophene)-alt-4,7-(2,1,3-benzo-thiadiazole)
- PDTPBT… Poly(2,6-(N-(1-octylnonyl)dithieno[3,2-b:20,30-d]pyrrole)-alt-4,7-(2,1,3-benzothiadiazole))
- PEDOT:PSS … Poly(3,4-ethylenedioxythiophene)-poly(styrenesulfonate)
- PET … Polyethylene terephthalate
- PSiF-DBT … Poly[2,7-(9,9-dioctyl-dibenzosilole)-alt-4,7-bis(thiophen-2yl)benzo-2,1,3-thiadiazole]
- TOPO … Trioctylphosphine oxide

6 Chemicals and Equipment

6.1 Chemicals

All chemicals were used as received.

- Acetone, 99%, Aldrich
- Acetonitrile, 99.8%, Aldrich
- Chlorobenzene, 99.9%, Aldrich
- Chloroform, 99.9%, Aldrich
- Copper(II)acetate, 99%, ABCR
- Copper(I)chloride, 97,0%, FlukaAG
- Copper(II)chloride, dihydrate 99%, ChemPUR
- Copper(I)iodide, 98%, Aldrich
- Copper(I)oxide, 97%, Aldrich
- Copper(II)oxide, 97%, Aldrich
- 1-Dodecanethiol, ≥97%, Fluka Analytical
- t-Dodecanethiol, mixture of isomers 98,5%, Aldrich
- 1,2-ethanedithiol, 98%, Fluka
- Ethanol, absolute, Baker
- Hexamethyldisilathiane, purum, Fluka
- Hexane, 95%, Roth
- Indium(III)acetate, 99.99%, Aldrich
- Indium(III)chloride, anhydrous 99.99%, ChemPUR
- Indium(III)oxide, 100%, Merck
- Isopropanol, 99.9%, Aldrich
- ITO covered glass substrates, Xin Yan Technology Limited
- Methanol, ≥99%, Baker
- 1-Octadecene, 90%, Aldrich
- Oleic Acid, 90%, Aldrich
- Oleylamine, 70%, Aldrich
- PEDOT:PSS for BHJ cells, Clevios PVP. Al 4083, Heraeus
- PEDOT:PSS for inverse BHJ cells, Clevios HTL Solar, Heraeus
- PSiF-DBT, 1-Material
- Toluene, 99.9%, Aldrich

- Trioctylphosphine oxide, 99%, Aldrich

6.2 Equipment

- UV/VIS Spectrometer Shimadzu UV 1800
- UV/VIS Spectrometer PerkinElmer Lambda 35
- Ultrasonic bath: VWR Ultrasonic Cleaner
- Profilometer: Bruker Dektak XT
- Plasma cleaning system: Diener electronics Femto
- Doctor blade: Ericksen Coatmaster 509 MC
- Diffractometer: Siemens D501
- Diffractometer: Bruker D8 Advance
- Simultaneous thermal analyzer: Netzsch Jupiter 449 C
- Flourescence Spectrophotometer: Hitachi F-7000
- Spin coater: Karl Suss Technique S.A. CT62
- Spin coater: SPI supplies KW-4
- Centrifuge: Hermle Z 323 K
- Source Measure Unit: Keithley 2400
- Glovebox: MBraun Labmaster DP
- Rate/Thickness Monitor for evaporation chamber: Inficon SQM 160
- Solar Simulator: Dedolight 400 D
- Heating plate: Heidolph MR Hei-Standard
- Infrared Spectrometer: Bruker, ALPHA

7 Literature

1. Moulé AJ, Chang L, Thambidurai C, Vidu R, Stroeve P. Hybrid solar cells: basic principles and the role of ligands. *J Mater Chem*. 2012;22(6):2351. doi:10.1039/c1jm14829j.

2. Rath T, Trimmel G. In situ syntheses of semiconducting nanoparticles in conjugated polymer matrices and their application in photovoltaics. *Hybrid Mater*. 2014;1(1):15-36. doi:10.2478/hyma-2013-0003.

3. U.S. Energy Information Administration. International Energy Outlook 2013. 2013.

4. European Comission eurostat. Renewable energy statistics, statistics explained. 2014. Available at: http://epp.eurostat.ec.europa.eu/statistics_explained/index.php/Renewable_energy_statistics#Source_data_for_tables_and_figures_.28MS_Excel.29.

5. Kalogirou S a. Solar thermal collectors and applications. *Prog Energy Combust Sci*. 2004;30(3):231-295. doi:10.1016/j.pecs.2004.02.001.

6. U.S. Department of Energy. *The History of Solar Technology*. Pennyhill Press; 2013.

7. Wagemann Hans-Günther EH. *Photovoltaik Solarstrahlung Und Halbleitereigenschaften, Solarzellenkonzepte Und Aufgaben*. 2nd editio. wiesbaden: Vieweg+Teubner; 2010.

8. P. RJ. *Science and Technology of Photovoltaics*. second edi. Leiden: CRC Press/Balkema, Taylor&Francis Group; 2010.

9. Wiberg N. *Lehrbuch Der Anorganischen Chemie*. 102nd ed. Berlin: Walter de Gruyter & Co.; 2007.

10. Atkins WP. *Kurzlehrbuch Physikalische Chemie*. Heidelberg, Berlin, Oxford: Spektrum Akademischer Verlag; 1993.

11. Mertens K. *Photovoltaik Lehrbuch Zu Grundlagen, Technologie Und Praxis*. Karl Hanser Verlag GmbH & Co. KG; 2011.

12. Günes S, Sariciftci NS. Hybrid solar cells. *Inorganica Chim Acta*. 2008;361(3):581-588. doi:10.1016/j.ica.2007.06.042.

13. Green MA, Emery K, Hishikawa Y, Warta W, Dunlop ED. Solar cell efficiency tables (version 43). 2014;(version 43):1-9. doi:10.1002/pip.

14. Xiang H, Wei S. Identifying Optimal Inorganic Nanomaterials for Hybrid Solar Cells. *J Phys Chem*. 2009:18968-18972.

15. Fradler C, Rath T, Dunst S, et al. Flexible polymer / copper indium sulfide hybrid solar cells and modules based on the metal xanthate route and low temperature annealing. *Sol Energy Mater Sol Cells*. 2014;124:117-125. doi:10.1016/j.solmat.2014.01.043.

16. Wright M, Uddin A. Organic—inorganic hybrid solar cells: A comparative review. *Sol Energy Mater Sol Cells*. 2012;107:87-111. doi:10.1016/j.solmat.2012.07.006.

17. Zhou R, Xue J. Hybrid polymer-nanocrystal materials for photovoltaic applications. *Chemphyschem*. 2012;13(10):2471-80. doi:10.1002/cphc.201101016.

18. Liu Z, Sun Y, Yuan J, et al. High-efficiency hybrid solar cells based on polymer/PbSx Se1-x nanocrystals benefiting from vertical phase segregation. *Adv Mater*. 2013;25(40):5772-8. doi:10.1002/adma.201302340.

19. Spanggaard H, Krebs FC. A brief history of the development of organic and polymeric photovoltaics. *Sol Energy Mater Sol Cells*. 2004;83(2-3):125-146. doi:10.1016/j.solmat.2004.02.021.

20. Nunzi J. Organic photovoltaic materials and devices. *Physique*. 2002;3:523-542.

21. Saunders BR, Turner ML. Nanoparticle-polymer photovoltaic cells. *Adv Colloid Interface Sci*. 2008;138(1):1-23. doi:10.1016/j.cis.2007.09.001.

22. Sun C, Wu Y, Zhang W, Jiang N, Jiu T, Fang J. Improving Efficiency by Hybrid TiO 2 Nanorods with 1,10- Phenanthroline as A Cathode Buffer Layer for Inverted Organic Solar Cells. 2014.

23. Scharber MC, Mühlbacher D, Koppe M, et al. Design Rules for Donors in Bulk-Heterojunction Solar Cells—Towards 10 % Energy-Conversion Efficiency. *Adv Mater*. 2006;18(6):789-794. doi:10.1002/adma.200501717.

24. Mertens K. *Photovoltaik Lehrbuch Zu Grundlagen, Technologie Und Praxis*. 2nd Editio. Carl Hanser Verlag GmbH & Co. KG; 2013:298.

25. Zhou R, Stalder R, Xie D, et al. Enhancing the efficiency of solution-processed polymer:colloidal nanocrystal hybrid photovoltaic cells using ethanedithiol treatment. *ACS Nano*. 2013;7(6):4846-54. doi:10.1021/nn305823w.

26. Rath T, Edler M, Haas W, et al. A Direct Route Towards Polymer/Copper Indium Sulfide Nanocomposite Solar Cells. *Adv Energy Mater*. 2011;1(6):1046-1050. doi:10.1002/aenm.201100442.

27. Reynolds LX, Lutz T, Dowland S, MacLachlan A, King S, Haque S a. Charge photogeneration in hybrid solar cells: a comparison between quantum dots and in situ grown CdS. *Nanoscale*. 2012;4(5):1561-4. doi:10.1039/c2nr12081j.

28. Kolny-Olesiak J, Weller H. Synthesis and application of colloidal CuInS2 semiconductor nanocrystals. *ACS Appl Mater Interfaces*. 2013;5(23):12221-37. doi:10.1021/am404084d.

29. Zhong H, Zhou Y, Ye M, et al. Controlled Synthesis and Optical Properties of Colloidal Ternary Chalcogenide CuInS2 Nanocrystals. *Chem Mater*. 2013;(c):6434-6443.

30. Aldakov D, Lefrançois A, Reiss P. Ternary and quaternary metal chalcogenide nanocrystals: synthesis, properties and applications. *J Mater Chem*. 2013;1(24):3756. doi:10.1039/c3tc30273c.

31. Arici BE, Sariciftci NS, Meissner D. Hybrid Solar Cells Based on Nanoparticles of CuInS2 in Organic Matrices **. 2003;(2):165-171.

32. Omata T, Nose K, Otsuka-Yao-Matsuo S. Size dependent optical band gap of ternary I-III-VI 2 semiconductor nanocrystals. *J Appl Phys*. 2009;105(7):073106. doi:10.1063/1.3103768.

33. Uehara M, Watanabe K, Tajiri Y, Nakamura H, Maeda H. Synthesis of CuInS2 fluorescent nanocrystals and enhancement of fluorescence by controlling crystal defect. *J Chem Phys*. 2008;129(13):134709. doi:10.1063/1.2987707.

34. Krause C, Miranti R, Witt F, et al. Charge transfer and recombination in organic / inorganic hybrid composites with CuInS 2 nanocrystals studied by light-induced electron spin resonance. *Sol Energy Mater Sol Cells*. 2014;124:241-246.

35. Liu Z, Wang L, Hao Q, et al. Facile synthesis and characterization of CuInS2 nanocrystals with different structures and shapes. *CrystEngComm*. 2013;15(36):7192. doi:10.1039/c3ce40631h.

36. Celik D, Krueger M, Veit C, et al. Performance enhancement of CdSe nanorod-polymer based hybrid solar cells utilizing a novel combination of post-synthetic nanoparticle surface treatments. *Sol Energy Mater Sol Cells*. 2012;98:433-440. doi:10.1016/j.solmat.2011.11.049.

37. Chen B, Zhong H, Zhang W, et al. Highly Emissive and Color-Tunable CuInS2-Based Colloidal Semiconductor Nanocrystals: Off-Stoichiometry Effects and Improved Electroluminescence Performance. *Adv Funct Mater*. 2012;22(10):2081-2088. doi:10.1002/adfm.201102496.

38. Hines M a., Scholes GD. Colloidal PbS Nanocrystals with Size-Tunable Near-Infrared Emission: Observation of Post-Synthesis Self-Narrowing of the Particle Size Distribution. *Adv Mater*. 2003;15(21):1844-1849. doi:10.1002/adma.200305395.

39. Mourdikoudis S, Liz-Marzan LM. Oleylamine in Nanoparticle Synthesis. *Chem Mater*. 2013.

40. Chang J, Waclawik ER. Controlled synthesis of CuInS2, Cu2SnS3 and Cu2ZnSnS4 nano-structures: insight into the universal phase-selectivity mechanism. *CrystEngComm*. 2013;15(28):5612. doi:10.1039/c3ce40284c.

41. Nam D-E, Song W-S, Yang H. Noninjection, one-pot synthesis of Cu-deficient CuInS2/ZnS core/shell quantum dots and their fluorescent properties. *J Colloid Interface Sci*. 2011;361(2):491-6. doi:10.1016/j.jcis.2011.05.058.

42. Li L, Daou TJ, Texier I, et al. Highly Luminescent CuInS 2 / ZnS Core / Shell Nanocrystals : Cadmium-Free Quantum Dots for In Vivo Imaging. 2009;(18):2422-2429.

43. Wu N, Fu L, Su M, Aslam M, Wong KC, Dravid VP. Interaction of Fatty Acid Monolayers with Cobalt Nanoparticles. *Nano Lett*. 2004;4(2):383-386. doi:10.1021/nl035139x.

44. Arar M, Haas W, Hofer F, et al. Comparing Photovoltaic Parameters of Conventional Cathodes with a Novel Silver Nanoparticle / Aluminum Cathode in Polymer Based Solar Cells. 2013;(3):3222-3225.

45. Greenham N, Peng X, Alivisatos a. Charge separation and transport in conjugated-polymer/semiconductor-nanocrystal composites studied by photoluminescence quenching and photoconductivity. *Phys Rev B*. 1996;54(24):17628-17637. doi:10.1103/PhysRevB.54.17628.

46. Nam M, Park J, Kim S-W, Lee K. Broadband-absorbing hybrid solar cells with efficiency greater than 3% based on a bulk heterojunction of PbS quantum dots and a low-bandgap polymer. *J Mater Chem A*. 2014;2(11):3978. doi:10.1039/c3ta15055k.

47. Radychev N, Lokteva I, Witt F, Kolny-Olesiak J, Borchert H, Parisi J. Physical Origin of the Impact of Different Nanocrystal Surface Modifications on the Performance of CdSe/P3HT Hybrid Solar Cells. *J Phys Chem C*. 2011;115(29):14111-14122. doi:10.1021/jp2040604.

48. Radychev N, Scheunemann D, Kruszynska M, et al. Investigation of the morphology and electrical characteristics of hybrid blends based on poly(3-hexylthiophene) and colloidal CuInS2 nanocrystals of different shapes. *Org Electron*. 2012;13(12):3154-3164. doi:10.1016/j.orgel.2012.09.007.

49. Ming He, Feng Qiu ZL. Toward High-Performance Organic−Inorganic Hybrid Solar Cells; bringing conjugated polymers and inorganic NP in close contact. *J Phys Chem Lett*. 2013.

50. Lefrançois A, Couderc E, Faure-Vincent J, Sadki S, Pron A, Reiss P. Effect of the treatment with (di-)amines and dithiols on the spectroscopic, electrochemical and electrical properties of CdSe nanocrystals' thin films. *J Mater Chem*. 2011;21(31):11524. doi:10.1039/c1jm10538h.

8 List of Figures

9 List of Tables